Computers and Geotechnics 159 (2023) 105470

Contents lists available at ScienceDirect

Computers and Geotechnics

journal homepage: www.elsevier.com/locate/compgeo

# Implementation of extrinsic cohesive zone model (ECZM) in 2D finite-discrete element method (FDEM) using node binding scheme

Weibing Cai [a], Ke Gao [a,b,*], Shugang Ai [a], Min Wang [c], Y.T. Feng [d]

[a] Department of Earth and Space Sciences, Southern University of Science and Technology, Shenzhen 518055, Guangdong, China
[b] Guangdong Provincial Key Laboratory of Geophysical High-resolution Imaging Technology, Southern University of Science and Technology, Shenzhen 518055, Guangdong, China
[c] T-3 Fluid Dynamics and Solid Mechanics Group, Theoretical Division, Los Alamos National Laboratory, Los Alamos 87545, NM, USA
[d] Zienkiewicz Centre for Computational Engineering, Faculty of Science and Engineering, Swansea University, Swansea, Wales, SA1 8EP, UK

ARTICLE INFO

*Keywords:*
Combined finite-discrete element method (FDEM)
Cohesive element
Extrinsic cohesive zone model (ECZM)
Intrinsic cohesive zone model (ICZM)
Node binding scheme
Rock fracturing simulations

ABSTRACT

The combined finite-discrete element method (FDEM) has been widely used for rock fracturing simulations. Conventionally, FDEM is realized using the intrinsic cohesive zone model (ICZM); however, it has the drawback of artificial compliance and high computational expense. As a complement, the extrinsic cohesive zone model (ECZM) is seen to be realized in FDEM recently, whereas the node splitting scheme utilized is cumbersome. Here, within the framework of ICZM-based FDEM, we propose a node binding scheme to efficiently bind the pre-discretized finite elements and thus guarantee the continuum behavior of materials in the elastic stage. The yield surfaces, controlled by ECZM, are dynamically embedded by invoking the pre-inserted cohesive elements. The effectiveness and efficiency of the proposed approach are validated and tested by performing a suite of numerical experiments. Compared with ICZM-based FDEM, the proposed approach can correctly capture material deformation and reduce the computation cost. In contrast to the existing ECZM-based FDEM, the proposed approach can overcome the frequent and complex element topology updating. This work provides a novel perspective that fully inherits the advantages of both ICZM and ECZM, but circumvents their shortcomings, which guarantees a more efficient and effective simulation of brittle material evolution from continuum to discontinuum.

## 1. Introduction

Since the pioneering work by Griffith (1920), fracture mechanics and damage mechanics have been extensively utilized in the fracturing analysis of brittle materials such as rocks. However, due to the inherent heterogeneity and anisotropy in rocks, the process of sub-critical and microcosmic crack propagation (see Fig. 1a) cannot be completely elucidated by such analytical approaches. Although a large number of laboratory experiments have been further performed to qualitatively and quantitatively investigate the mechanism of crack initiation, propagation and coalescence in rocks (Li et al. 2020; Wei et al. 2020), experimental results are greatly influenced by testing conditions such as specimen preparation, equipment accuracy and loading conditions. Any variation in the experimental process may yield different or even contradictory fracturing results.

As a powerful complement to analytical and experimental methods, numerical simulations, owing to their rapidity and convenience, have been extensively employed in recent years to investigate the fracturing mechanism of rocks (Deng et al. 2021c; Duan et al. 2019; Euser et al. 2019; Lisjak et al. 2017; Lisjak et al. 2013; Liu et al. 2018; Munjiza et al. 2013). Generally, numerical approaches can be classified into three categories, i.e., continuum-based, discontinuum-based, and hybrid (combination of continuum- and discontinuum-based) approaches. Continuum-based approaches, such as the finite element method (FEM) (Ortiz and Structures 1988), boundary element method (BEM) (Aliabadi 1997), extended finite element method (XFEM) (Belytschko et al. 2001), material point method (MPM) (Junior and Cheng 2013), peridynamics (PD) (Silling and Askari 2005) and phase field (PF) (Francfort and Marigo 1998), have difficulties in explicitly simulating the separation and healing of crack surfaces effectively. Discontinuum-based approaches, for example, the discrete element method (DEM, with bonds) (Cundall and Strack 1979) and discontinuous deformation analysis

* Corresponding author.
*E-mail address:* gaok@sustech.edu.cn (K. Gao).

https://doi.org/10.1016/j.compgeo.2023.105470
Received 28 October 2022; Received in revised form 16 February 2023; Accepted 6 April 2023
0266-352X/© 2023 Elsevier Ltd. All rights reserved.

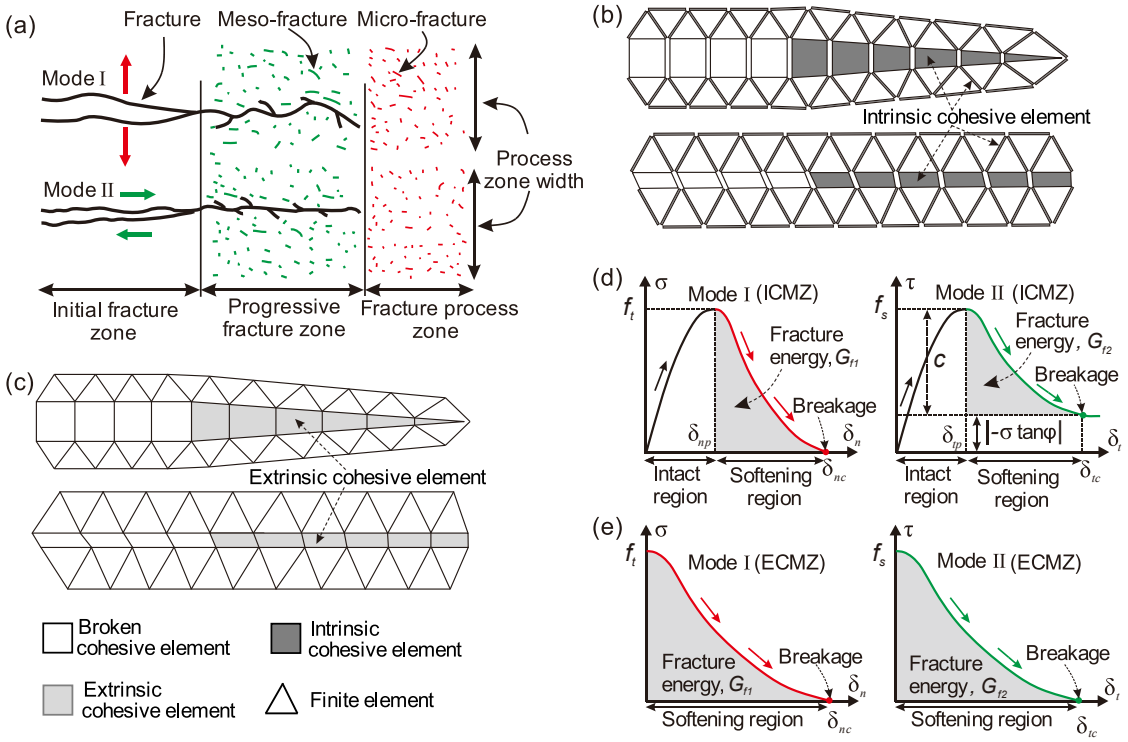


**Fig. 1.** Material fracturing modeling in dFDEM and cFDEM, respectively. (a) Conceptual model of FPZ (fracture process zone) development ahead of fracture tip in brittle material (modified from Mohammadnejad et al. 2018). The implementation of FPZ in Mode I and II in (b) dFDEM and (c) cFDEM. (d) ICZM for Mode I and II. (e) ECZM for Mode I and II. The $G_{f1}$ and $G_{f2}$ denote the Mode I and II fracture energy, respectively; $c$ and φ represent the cohesion and internal friction angle, respectively; σ and τ are the tensile and shear stress of cohesive elements, respectively; $f_t$ and $f_s$ are the tensile and shear strength, respectively; $\delta_{np}$ and $\delta_{tp}$ are the elastic limits of the normal and tangential separations, respectively; $\delta_{nc}$ and $\delta_{tc}$ are the maximum tensile and shear separation, respectively.

(DDA) (Shi and Goodman 1985), fail to accurately capture and estimate the deformation and stress distribution in solids due to the lack of theoretical basis of continuum mechanics. Particularly, the fracture morphology and porosity are poorly characterized in particle-based DEM due to unavoidable gaps between particles. The hybrid methods, such as the numerical manifold method (NMM) (Shi 1992), continuum-based discrete element method (CDEM) (Ju et al. 2016) and the combined finite-discrete element method (FDEM) (Munjiza 1992), because of their capability of capturing the deformation of continuum and the interaction between discrete objects, have proved to be superior to pure continuum-based or discontinuum-based approaches. However, not all hybrid models are capable of adequately modeling the progressive fracturing and failure progress of brittle rocks.

As a typical hybrid approach originally proposed by Munjiza (Munjiza 1992), the FDEM, which merges FEM-based analysis of continua with DEM-based contact processing for discontinua, provides an effective solution to simulate the fracturing behavior in rocks (Munjiza 2004). Conventionally, the FDEM is realized using the intrinsic cohesive zone model (ICZM) with a traction-separation law, in which the modeling domain is first discretized into a series of finite elements. Then cohesive elements with zero initial thickness are inserted into the common boundaries between adjacent finite elements prior to the simulation. The finite elements can capture the deformation of the solid domain, and the intrinsic cohesive elements are responsible for simulating the inter-element crack initiation, propagation and coalescence (see Fig. 1b). Both types of elements participate in the computation from the beginning of the simulation. Because of the existence of an initial elastic stage in the traction-separation law of ICZM (see Fig. 1d), the intrinsic cohesive elements also sustain part of the material deformation before fracture onset. To reduce local stress oscillation induced by the non-smooth transition from cohesive element to contact in terms of nodal force calculation especially when compressive-shear fractures are generated, the brute-force contact activation is commonly adopted in most existing FDEM realizations, in which all finite elements are added to the contact list from the onset of the simulation (Deng et al. 2021a). However, such an early participation of finite elements in contact calculation (even during the elastic deformation regime) would no doubt increase the computational cost. As an improvement, a semi-adaptive contact activation approach is recently proposed in which the contact interaction between adjacent finite elements is only invoked when the corresponding cohesive element is completely broken (Fukuda et al. 2021).

Because finite elements and intrinsic cohesive elements use different types of constitutive laws, they deform at different rates even in the elastic deformation stage, and thus may cause discontinuous strains across adjacent finite elements and make the originally continuous model domain behave like a discontinuum before fracture onset. Essentially, such a common ICZM-based FDEM realization is more discontinuum-oriented, and for easy reference, it is referred to as "dFDEM" hereafter. Due to its ease of implementation, dFDEM is increasingly popular and has been incorporated into many commercial and research codes such as ABAQUS (Jiang et al. 2020), Y-code (Munjiza 2004), Y-Geo (Lisjak et al. 2018), HOSS (Euser et al. 2019), Irazu (Mahabadi et al. 2012), Y-HFDEM (Liu et al. 2015), Solidity (Lei et al. 2016) and MultiFracS (Yan et al. 2021). To date, the dFDEM has been widely used in many aspects of rock mechanics for fracturing-related analyses from laboratory to engineering field scale, such as blasting (Han et al. 2020b; Wang et al. 2021), discrete fracture network (Lei and Gao 2018; Lei et al. 2021a), tunnel excavation (Han et al. 2020a), acoustic emission monitoring (Lisjak et al. 2013; Zhao et al. 2014; Zhao et al. 2015) and multi-physics/field coupling (Yan et al. 2018; Yan et al. 2022).

Nevertheless, since the inherent stiffness difference between the intrinsic cohesive elements and the solid finite elements, the dFDEM usually yields a smaller overall material elastic modulus than the true value, i.e., stiffness reduction, or the so-called artificial compliance

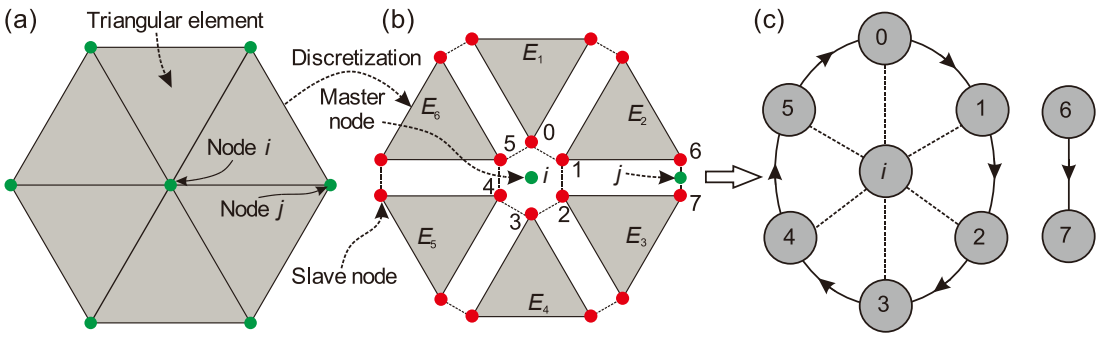


**Fig. 2.** Mesh discretization and re-join of triangular finite elements by cohesive elements. Nodes 0 to 5 are slave nodes and are bound together as a group identified by a master Node *i* located inside the model; similarly, slave nodes 6 and 7 are also bound together and identified by another master Node *j* located on the model boundary. The triangular finite elements are marked as $E_1$, $E_2$, $E_3$, $E_4$, $E_5$ and $E_6$ in clockwise order.

problem (Xu et al. 2022) (as will be detailed in Section 4.1). For a similar reason, the dFDEM could produce larger fracture apertures than the real one (as will be proved in Section 4.2), which may cause significant inaccuracy in fluid–solid coupling problems such as hydraulic fracturing simulation due to the sensitivity of fluid pressure to fracture aperture (Lisjak et al. 2017; Yan and Jiao 2018; Yan et al. 2018). To alleviate such an artificial compliance problem, a larger intrinsic cohesive element stiffness has to be employed during the elastic stage, which no doubt will decrease the modeling time step and thus increase the computational expense (Tatone and Grasselli 2015). Together with the fact that all cohesive elements, which are at least 1.5 (in 2D) or 2 (in 3D) times of the solid finite elements, participate in the computation from the beginning of the simulation, the conventional dFDEM is unquestionably a computationally expensive approach (Deng et al. 2021d; Lisjak et al. 2014; Liu and Deng 2019; Yan et al. 2018).

To overcome the aforementioned deficiencies in conventional dFDEM, Fukuda et al. (2020) recently introduced the extrinsic cohesive zone model (ECZM) in FDEM for inter-element fracturing simulation, where cohesive elements are adaptively inserted between adjacent finite elements based on a stress-based strength criterion (see Fig. 1c). Different from the intrinsic cohesive elements, the extrinsic cohesive elements directly enter the strain-softening stage after insertion and do not bear material elastic deformation (see Fig. 1e), which guarantees the continuum behavior of numerical models prior to fracture onset and thus can readily avoid the artificial compliance problem in dFDEM. Compared with dFDEM, this type of FDEM realization is more continuum-oriented, and is thus abbreviated as "cFDEM" hereafter. Since the computation of cohesive elements is not needed in the elastic stage, cFDEM is theoretically less computationally intensive and could generate more reasonable results than dFDEM. However, the adaptive insertion of cohesive elements during the simulation is very challenging, which requires a robust splitting of local nodes between adjacent finite elements and a frequent update of the topology information of related elements. The node splitting scheme cannot be straightforwardly achieved, especially in 3D simulations due to the more complicated spatial topological connection between elements, and it can also introduce considerable computation overhead (Fukuda et al. 2021). Additionally, the complexity of the node splitting scheme in such cFDEM realization could increase the difficulty in code parallelization and may reduce the computational stability compared with dFDEM.

To circumvent the disadvantages of the conventional ICZM-based dFDEM and the existing ECZM-based cFDEM using node splitting scheme, we propose a novel implementation of ECZM in 2D FDEM using node binding scheme based on our in-house FDEM code – Pamuco (**Pa**rallel • **mu**ltiphysics • **co**upling). Specifically, similar to dFDEM, we first discretize the numerical model domain into finite elements and rejoint them with zero-thickness cohesive elements; then, instead of splitting nodes such that in the existing cFDEM, we use a node binding scheme, in a master–slave manner, to bind nodes that share the same original coordinates during the elastic deformation stage. The proposed cFDEM realization suppresses the calculation of cohesive elements prior to fracture onset, which ensures the continuum behavior of the model domain in the elastic stage. When a certain strength criterion is reached, the pre-inserted cohesive element will be invoked and enter the strain-softening stage like that in ECZM. Meanwhile, the node binding lists will be automatically updated to accommodate the explicit separation of fracture surfaces. Essentially, the proposed cFDEM inherits the merits of both ICZM and ECZM, but avoids their shortcomings. That is, it generates reasonable results like the existing ECZM-based cFDEM, but evades its challenging node splitting and frequent updating of element topology information. Additionally, since no cohesive element computation is needed during the elastic stage, the proposed cFDEM could reduce the computational cost substantially.

The paper is organized as follows. In Section 2, we introduce the fundamental principles of FDEM and our proposed node binding scheme. In Section 3, a series of benchmark cases are performed to validate the proposed cFDEM. Then, the advantages of cFDEM over dFDEM are demonstrated in Section 4 in terms of simulated model stiffness, generated fracture aperture and computational efficiency. Conclusions are drawn in Section 5.

## 2. Formulations of the proposed cFDEM

In this section, we first briefly illustrate the governing equations and the calculation of Cauchy stress in FDEM. Then, the proposed node binding scheme is introduced, which ensures the equivalent continuum behavior of the model domain in the elastic deformation stage. Following this, we demonstrate the realization of fracture initiation and propagation in the proposed cFDEM.

### 2.1. Governing equations and stress–strain formulation

The FDEM uses an explicit time integration scheme to solve the motion equations and to update the velocity and displacement of each node at each time step. The governing equation is (Munjiza 2004)

$$\mathbf{M}\ddot{\mathbf{x}}(t) + \mathbf{C}\dot{\mathbf{x}}(t) = \mathbf{f} \tag{1}$$

where $\mathbf{M}$ is the nodal mass matrix, $\mathbf{C}$ is the damping matrix, $\mathbf{x}$ is the nodal displacement vector, $\ddot{\mathbf{x}}$ and $\dot{\mathbf{x}}$ are the nodal acceleration and velocity vectors, respectively, and $\mathbf{f}$ represents the total force vector. The mechanical behavior of constant strain finite elements can be expressed by (Munjiza 2004)

$$\sigma_{ij} = \frac{\lambda}{2}\left(J - \frac{1}{J}\right)\delta_{ij} + \frac{\mu}{J}\left(\mathrm{B}_{ij} - \delta_{ij}\right) + \eta \mathrm{D}_{ij} \quad (i,j = 1, 2) \tag{2}$$

where $\sigma_{ij}$ represents the Cauchy stress tensor, $\lambda$ and $\mu$ are the Lame constants, $\mathrm{B}_{ij}$ denotes the left Cauchy-Green strain, $\mathrm{D}_{ij}$ is the rate of

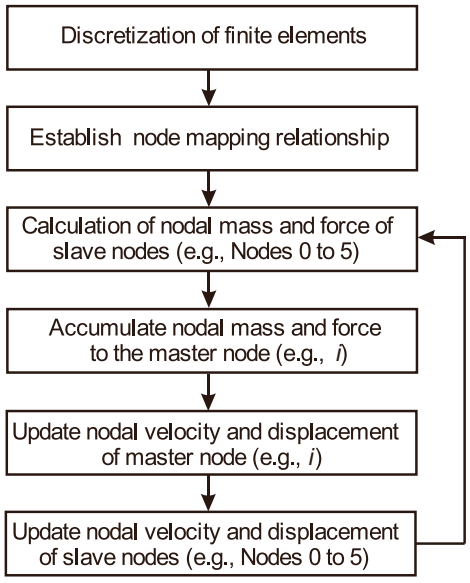


**Fig. 3.** Workflow of elastic deformation computation in the proposed cFDEM.

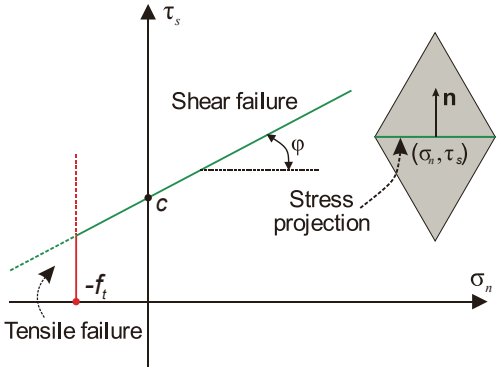


**Fig. 4.** Schematic of the Mohr-Coulomb and maximum tensile strength criterion. $\sigma_n$ and $\tau_s$ are the normal and tangential stress resolved along the cohesive element, respectively; $c$ and $\varphi$ denote the material cohesion and internal friction angle, respectively; $f_t$ is the tensile strength. The inner normal direction of the cohesive element is denoted by $\mathbf{n}$.

deformation tensor, $J$ is the determinant of deformation gradient, $\eta$ is the viscous damping coefficient, and $\delta_{ij}$ is the Kronecker delta. The $B_{ij}$ and $D_{ij}$ are calculated by deformation gradient and velocity gradient, respectively.

### 2.2. Elastic deformation and node binding scheme

To inherit the advantages of the existing ECZM-based cFDEM for material deformation simulation in the elastic stage and to avoid its challenging and frequent updating of element topology information when new fractures are initiated, in the proposed realization of cFDEM, we first borrow the strategies used in the ICZM-based dFDEM for element topology processing. Taking the model presented in Fig. 2 for example, before the simulation, we discretize the whole continuous model domain into six triangular finite elements (Fig. 2a), and then separate them into independent ones (without node sharing) and re-joint adjacent finite elements with four-node zero-thickness cohesive elements (Fig. 2b, the cohesive element thickness is exaggerated for better visualization). We retain the new topology information of both finite elements and cohesive elements after model discretization.

To prepare for the node binding scheme in a later stage, during the model discretization procedure, we also reserve the mapping information from the original nodes before model discretization (denoted as master nodes, e.g., Node $i$ in Fig. 2a) to the corresponding new nodes after model discretization (denoted as slave nodes, e.g., Nodes 0 to 5 in Fig. 2b) in a master–slave manner. Each master node corresponds to several slave nodes, forming a master–slave group. This mapping information between the master and slave nodes can be saved in a list such as $0 \rightarrow i$, $1 \rightarrow i$, …, $5 \rightarrow i$ (Fig. 2c). If a master node is located inside the model (i.e., not connected to any model boundaries, e.g., Node $i$), all its slave nodes will be stored in a circular linked list according to their relative positions, e.g., $0 \rightarrow 1 \rightarrow 2 \rightarrow 3 \rightarrow 4 \rightarrow 5 \rightarrow 0$ (Fig. 2c). However, if a master node is located on the model boundary (e.g., Node $j$), its slave nodes (e.g., Nodes 6, 7) can be stored in an open linked list, e.g., $6 \rightarrow 7$. It is worth noting that the master nodes from the original mesh are merely used as identifiers for each slave node group. After model discretization, the original mesh topology information will be abandoned, and all later computations will be conducted only based on the new element topology.

To avoid the discontinuous elastic deformation similar to that in the ICZM-based dFDEM caused by the different stiffness between finite elements and cohesive elements, we suppress the functionality of pre-inserted cohesive elements (i.e., they will not participate in the computation) during the elastic stage by binding the slave nodes in each group. In other words, the slave nodes in the same group will displace together with their master node and share identical coordinates, which guarantees pure continuous deformation in areas without yield surfaces (i.e., the cohesive elements entered into the strain-softening stage) or fractures (i.e., the complete breakage of cohesive elements). Specifically, in each iteration (one time step), during the simulation, after calculating the nodal parameters (e.g., displacement and velocity) in each finite element, based on the master–slave node group information constructed earlier, the nodal forces and nodal masses of slave nodes in each group are all accumulated to their master node. Then, the acceleration $\ddot{\mathbf{x}}_i(t)$ of the master node can be determined by Eq. (1), and its velocity $\dot{\mathbf{x}}_i(t+\Delta t)$ is updated by the central difference scheme (Munjiza 2004)

$$\dot{\mathbf{x}}_i(t+\Delta t) = \dot{\mathbf{x}}_i(t) + \ddot{\mathbf{x}}_i(t)\cdot\Delta t \tag{3}$$

where $\Delta t$ is the time step, and $t$ and $t+\Delta t$ denote the previous and current time instants, respectively. The coordinates $\mathbf{x}_i(t+\Delta t)$ of the master node can be updated by

$$\mathbf{x}_i(t+\Delta t) = \mathbf{x}_i(t) + \dot{\mathbf{x}}_i(t+\Delta t)\cdot\Delta t \tag{4}$$

At the end of each iteration, the velocities and coordinates of all slave nodes in the same group need to be synchronized as the same as their master node. The workflow for elastic deformation calculation in the proposed cFDEM is illustrated in Fig. 3. In contrast, in the framework of the ICZM-based dFDEM, the variables of each node are independently calculated and updated, which inevitably leads to different nodal velocities and coordinates among nodes that are supposed to have identical values, and thus results in the incompatible strain between adjacent finite elements. Additionally, our proposed node binding scheme avoids the time-consuming computation of cohesive elements during the elastic stage, and can save considerable computational costs.

### 2.3. Fracture initiation and propagation

Rock failure is a progressive damage process where microcracks are first initiated, and then gradually developed into meso- or macro-fractures (see Fig. 1a). To simulate fracture initiation and propagation, in our proposed cFDEM, the yield surfaces are dynamically embedded by invoking the pre-inserted cohesive elements when the strength criterion is reached. Here, we use the Mohr-Coulomb and maximum tensile strength criterion shown in Fig. 4 to simulate both the shear and tensile fractures. The cohesive element is invoked when both the Cauchy

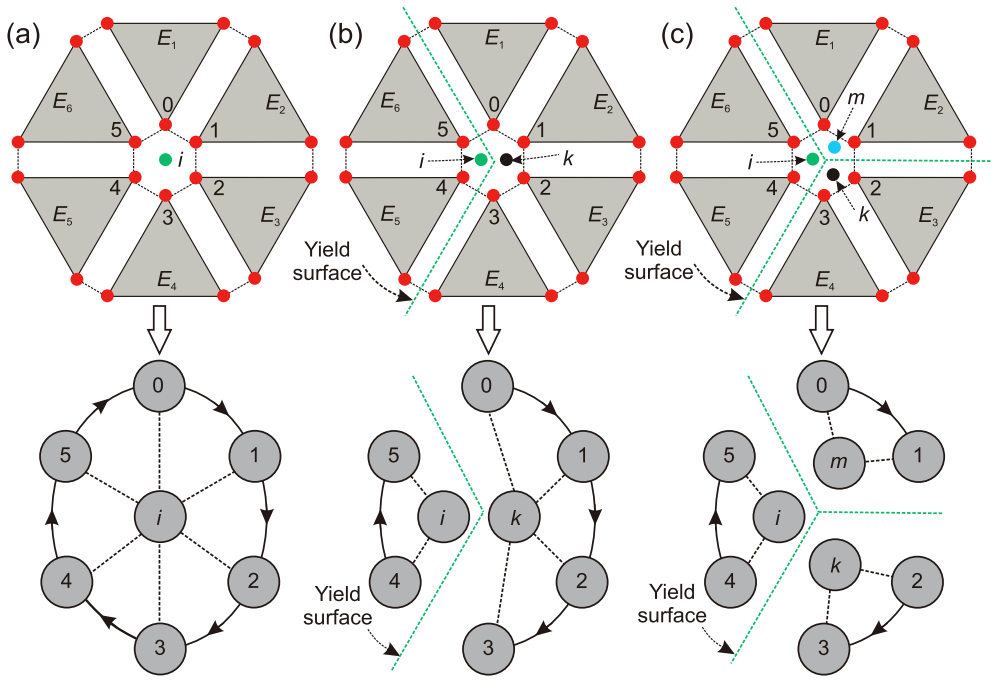


**Fig. 5.** Schematic of updating the master–slave node mapping list and slave node group linked lists when pre-inserted cohesive elements are invoked. The triangular finite elements are marked as $E_1$, $E_2$, $E_3$, $E_4$, $E_5$ and $E_6$ in clockwise order, and Nodes $i$, $k$ and $m$ are the master nodes used to bind the slave Nodes 0 to 5.

stresses of the two adjacent finite elements (calculated using Eq. (2)) resolved on their common edge (i.e., the common cohesive element) satisfy the following conditions:

$$\begin{cases} \sigma_n < -f_t, & \text{Tensile failure} \\ \tau_s > c + \sigma_n tan\varphi, & \text{Shear failure} \end{cases} \tag{5}$$

where $\sigma_n$ and $\tau_s$ are the normal and tangential stresses on the common edge, respectively; $f_t$ is the material tensile strength; $c$ and $\varphi$ denote the cohesion and internal friction angle, respectively. These material parameters are directly assigned to cohesive elements. The sign convention of tension as negative is used here. The tensile and shear cracks are initiated when the local stresses meet the tensile and shear strength, respectively. It is worth noting that other strength criteria can also be implemented in our proposed cFDEM framework to replace the Mohr-Coulomb and maximum tensile strength criterion.

It is pertinent to point out that when tensile failure occurs first while the shear stress has not reached the shear strength, the continuity of shear stress before and after activating the cohesive element is not well solved at the moment; similar problems exist for the continuity of tensile stress when shear failure occurs first. This is a challenging and long-lasting problem in cohesive element related approaches, as pointed out in previous studies (Fukuda et al. 2021; Knight et al. 2020; Papoulia et al. 2003; Sam et al. 2005). However, solving this problem is out of the scope of current work.

When a pre-inserted cohesive element is invoked and marked as a yield surface, the master–slave node mapping list and the two groups of slave node linked lists corresponding to the two master nodes related to the cohesive element need to be updated accordingly. This update ensures the independent computation of the elastic deformation of finite elements located on the two sides of the yield surface (or fracture, if the yield surface is broken later) and allows the relative displacement between the two edges of the cohesive element. Continuing with the example shown in Fig. 2 and focusing on the master Node $i$, once the cohesive element between Elements $E_4$ and $E_5$ becomes a yield surface, the connection between the slave Nodes 3 and 4 will be cut out, and the previous circular linked list becomes an open linked list, such as 4 → 5 → 0 → 1 → 2 → 3 (Fig. 5a); however, the slave Nodes 0 to 5 are still in the same group and mapped to the same master Node $i$ at this time, since they are located at a fracture tip inside the model and have to be enforced to displace together. As the model evolves and another cohesive element is invoked, say, the one between Elements $E_6$ and $E_1$, the connection between the slave Nodes 0 and 5 will again be cut out, and the previous open linked list becomes two open linked lists, i.e., 0 → 1 → 2 → 3 and 4 → 5 (Fig. 5b). Then, the slave Nodes 0 to 5 are divided into two groups, and they are respectively mapped to a new master Node $k$ and the old master Node $i$ (Fig. 5b). Further invocation of cohesive elements, e.g., the one between Elements $E_2$ and $E_3$ shown in Fig. 5c, can be realized by repeating the above procedure. The other nodes of these invoked cohesive elements should also be processed at the same time in a similar manner.

It can be seen that only when a slave node linked list to be cut out is an open list, i.e., the corresponding master node is either located on the model boundaries or connected to an existing yield surface, a new master node is needed to update the master–slave node mapping list and the slave node group lists. Otherwise, if a slave node linked list is a circular list, i.e., the corresponding master node must be located inside the model and not connected to any yield surfaces, we only need to break it into an open linked list, and no master–slave mapping information and slave node group information needs to be altered. Based on this straightforward rule, we can also avoid the constant and tedious checking of whether a node is at model boundaries like that in the existing ECZM-based cFDEM when conducting the node splitting procedure. Once the linked lists of slave node groups and the master–slave node mapping list are updated, they will be used to calculate the corresponding elastic deformation by iterating the node binding scheme presented in Section 2.2.

Upon the invocation of a cohesive element and the update of corresponding master–slave node lists, the cohesive element starts to participate in the computation and its mechanical behaviors are controlled by the traction-separation-based strain-softening laws of ECZM shown in Fig. 1e. After this, the two edges of the yield surface may displace relative to each other (i.e., open or slide) depending on the subjected stress conditions. Note that if a yield surface is an isolated one (i.e., not connected to any other yield surfaces) and not linked to any model boundaries, its two edges will have no relative displacement due

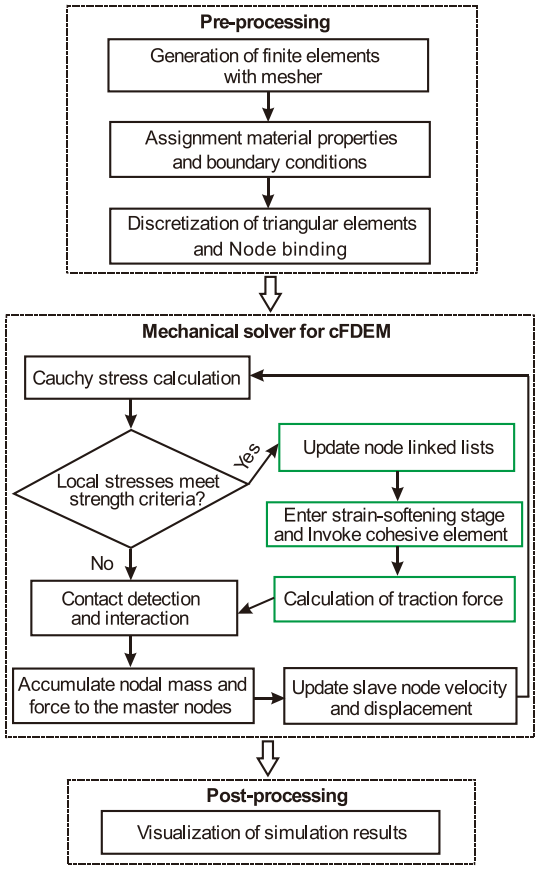


**Fig. 6.** Simulation workflow of the proposed cFDEM.

to the constraint of the node binding scheme acting on its two tips, although the relative displacement is technically allowed. In other words, the relative displacement of the two edges of a yield surface is possible only if it is either connected to a model boundary or linked to any other existing yield surfaces and forms a separable surface. However, in contrast to the existing ECZM-based cFDEM, we do not need to explicitly check whether a new yield surface can form a separable surface.

When a cohesive element enters the yield stage, the separation vector $\boldsymbol{\delta}$ quantifying the relative displacement of its two edges at any point is given by

$$\boldsymbol{\delta} = \delta_n \mathbf{n} + \delta_t \mathbf{t} \tag{6}$$

where $\mathbf{n}$ and $\mathbf{t}$ are the normal and tangential unit vectors that define a local coordinate system with respect to the yield surface, respectively (Lei et al. 2021b); $\delta_n$ and $\delta_t$ are the normal and tangential separations at any point on the yield surface, respectively. The local traction vector $\mathbf{p}$ can be represented by

$$\mathbf{p} = \sigma \mathbf{n} + \tau \mathbf{t} \tag{7}$$

where $\sigma$ and $\tau$ are the normal and tangential stresses in the direction of $\mathbf{n}$ and $\mathbf{t}$, respectively. Based on the strain-softening law in ECZM, the interfacial potential is defined as a function of the separation vector components as (Camacho and Ortiz 1996; Xu and Needleman 1993)

$$\mathbf{p} = \nabla\varphi(\delta_n, \delta_t) = \frac{\partial \varphi}{\partial \delta_n}\mathbf{n} + \frac{\partial \varphi}{\partial \delta_t}\mathbf{t} \tag{8}$$

where $\nabla$ denotes the gradient operator that is the spatial derivative of $\mathbf{n}$ and $\mathbf{t}$. For convenience, the interfacial potential can be further simplified as a function of an intermediate variable $\delta = \sqrt{\delta_n^2 + \delta_t^2}$, thus

$$\mathbf{p} = \nabla\varphi(\delta) = \left(\frac{\partial \delta}{\partial \delta_n}\mathbf{n} + \frac{\partial \delta}{\partial \delta_t}\mathbf{t}\right) f(\delta) \tag{9}$$

where,

$$f(\delta) = \frac{d\varphi(\delta)}{d\delta} \tag{10}$$

represents the shape of the strain-softening curve, which could be determined by laboratory experiments (Anyfantis and Tsouvalis 2012).

In this study, similar to other FDEM implementations (Deng et al. 2021b), we use three integration points (two endpoints and one middle point) on a yield surface to check the softening characteristics of a cohesive element, by balancing between computational efficiency and computational accuracy. A variable $d$ is defined at each integration point to characterize the damage evolution associated with the yield surface, i.e.,

$$d = \min\left(\sqrt{\left(\frac{\delta_n}{\delta_{nc}}\right)^2 + \left(\frac{\delta_t}{\delta_{tc}}\right)^2},\ 1\right) \tag{11}$$

where $\delta_{nc}$ and $\delta_{tc}$ are the maximum tensile and shear separations, respectively. The integration point on a cohesive element is completely damaged when $d = 1$. If three integration points are completely damaged, we deem that a new fracture is generated from the cohesive element (i.e., the complete breakage of the yield surface or cohesive element), and the fracture types (tensile or shear) are determined by the failure types. For tensile failure, we can obtain (Lei et al. 2021b)

$$\sigma = z(d) f_t \tag{12}$$

where $f_t$ is the tensile stress, and $z(d)$ denotes the heuristic softening function given by (Munjiza et al. 1999)

$$z(d) = \left[1 - \frac{A+B-1}{A+B}\exp\left(d\frac{A+CB}{(A+B)(1-A-B)}\right)\right] \times \left[A(1-d) + B(1-d)^C\right] \quad (0 \leqslant d \leqslant 1) \tag{13}$$

where $A$, $B$ and $C$ are intrinsic rock parameters (0.63, 1.8, and 6.0, respectively) that determine the shapes of the strain-softening curve. The Mode I fracture energy $G_{f1}$ can be represented by

$$G_{f1} = \int_0^{\delta_{nc}} \sigma \, \mathrm{d}\delta_n \tag{14}$$

For shear failure, we can also obtain the shear stress (Lei et al. 2021b) and Mode II fracture energy $G_{f2}$ by

$$\tau = z(d) f_s \tag{15}$$

and

$$G_{f2} = \int_0^{\delta_{tc}} \tau \, \mathrm{d}\delta_t \tag{16}$$

where $f_s$ is the shear strength.

During this strain-softening procedure for fracturing simulation, no node splitting and element topology update is needed in our proposed cFDEM. When new fractures are generated from the yield surfaces when all integration points are completely damaged ($d = 1$), the computation of the corresponding cohesive elements will be terminated. Then the finite elements on the two sides of the fractures are free to move and thus realize an explicit separation of fracture surfaces (i.e., strong discontinuities). Then, the interactions between the finite elements on the two sides of the fractures will be controlled by contact algorithms, which involve contact detection and contact interaction. The contact detection of whether finite elements at boundaries are in touch is conducted using the efficient NBS (non-binary search) algorithm, with its complexity

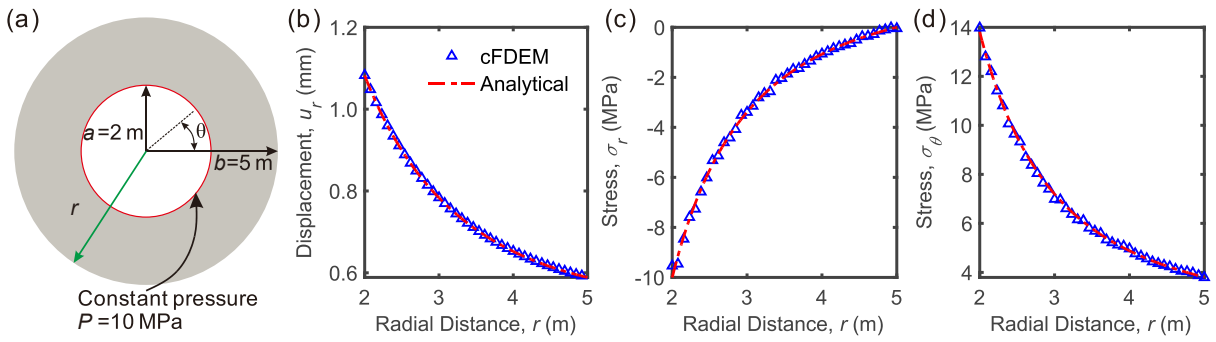


**Fig. 7.** (a) Model geometry of the hollow thick-wall cylinder. Comparison of (b) radial displacement, (c) radial stress and (d) tangential stress distribution in the cylinder between the analytical solution and the cFDEM simulated results.

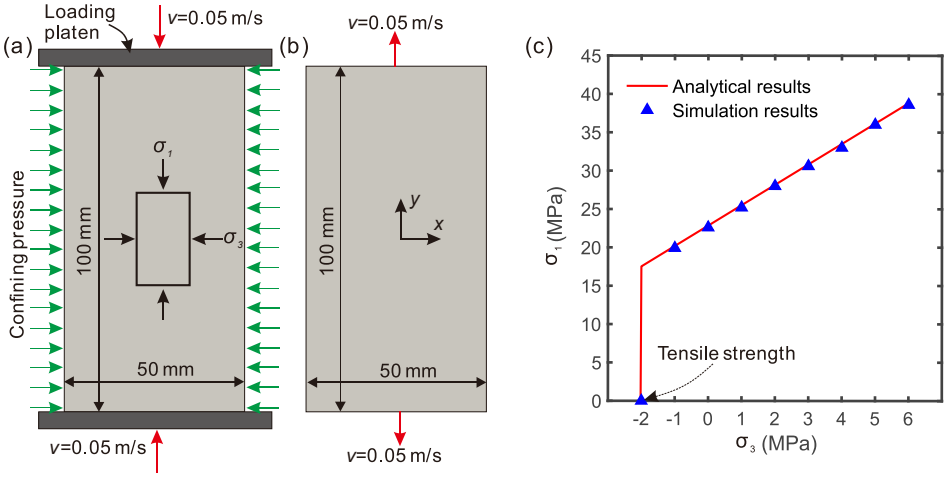


**Fig. 8.** Triaxial compression and direct tension tests. (a) Triaxial compression test. (b) Direct tension test. (c) Comparison between the cFDEM simulated $\sigma_1$-$\sigma_3$ relations and the theoretical curves of Mohr-Coulomb and maximum tensile strength criterion in principal stress space.

linearly proportional to the total number of contact couples (Munjiza and Andrews 1998). Regarding contact interaction, the calculation of normal contact force is based on the overlap area of contact couples, while the shear contact force is determined by their relative sliding displacement (Munjiza 2004). More details regarding the formulations of normal and tangential contact forces are demonstrated in Appendix A.

To summarize, the complete simulation workflow, including pre-processing, mechanical solver and post-processing in the proposed cFDEM, is presented in Fig. 6.

## 3. Validations of the proposed cFDEM

In this section, several specially designed numerical experiments are conducted to validate the proposed cFDEM. First, we adopt a thick-wall cylinder under constant inner pressure to validate the accuracy of cFDEM for elastic deformation and stress simulation. Then a series of triaxial compression and direct tension tests are performed to test the accuracy of the implementation of the Mohr-Coulomb and maximum tensile strength criterion. Finally, several representative benchmarks are utilized to validate the capability of the proposed cFDEM for fracture initiation and propagation simulation in models with a pre-existing flaw.

### 3.1. Internal pressurized hollow cylinder test

A thick-wall cylinder with an inner diameter $a = 2$ m and outer diameter $b = 5$ m is first used to test the correctness of the proposed cFDEM for elastic deformation simulation. The cylinder is assumed homogeneous and isotropic, and a pressure $P = 10$ MPa is applied to the inner boundary and the outer boundary is free to move (see Fig. 7a). The analytical solution for the displacement and stress distribution in the thick-wall cylinder under the plane stress condition is given by (Timoshenko and Goodier 1970)

$$\begin{cases} u_r = \dfrac{a^2}{E(b^2-a^2)r}\left((1-\nu)r^2+(1+\nu)b^2\right)P \\ \sigma_r = -\dfrac{b^2/r^2-1}{b^2/a^2-1}P \\ \sigma_\theta = \dfrac{b^2/r^2+1}{b^2/a^2-1}P \end{cases} \tag{17}$$

where $u$ and $\sigma$ respectively denote the displacement and stress, and the subscripts $r$ and $\theta$ represent the radial and angular directions, respectively, in the polar coordinate system. Here, $r$ starts from the cylinder center and $\theta$ is anti-clockwise positive from the right. We use Young's modulus $E = 30$GPa, Poisson's ratio $\nu = 0.27$ and viscous damping coefficient $\eta = 3.4 \times 10^5$ kg/m·s in the model, and the parameters used can guarantee that the model is still in the elastic deformation stage. Note that the calculation of viscous damping coefficient for finite elements can refer to previous work (Tatone and Grasselli 2015). The model consists of 35,028 triangular elements with an average element size of 0.1 m, and an unstructured Delaunay triangulation mesh scheme is utilized. The total simulation time is $9 \times 10^{-2}$ s with a time step of $9.0 \times 10^{-7}$ s. To maintain a stable pressure on the inner boundary, the pressure on the inner boundary is increased gradually from 0 to the prescribed value via a time span of $2 \times 10^{-2}$ s. The distributions of $u_r$, $\sigma_r$ and $\sigma_\theta$ with respect to $r$ from both the analytical solution and the proposed cFDEM

**Table 1**
Input parameters in cFDEM model for triaxial compression and direct tension tests (Liu and Deng 2019).

| Input parameters | Values |
|---|---|
| Young's modulus, $E$ (GPa) | 12.5 |
| Bulk density, ρ (kg/m$^3$) | 2400 |
| Poisson's ratio, $\nu$ | 0.25 |
| Viscous damping coefficient, η (kg/m·s) | 5500 |
| Tensile strength, $f_t$ (MPa) | 2 |
| Cohesion, $c$ (MPa) | 7 |
| Internal friction angle, φ (°) | 27 |
| Mode I fracture energy, $G_{f1}$ (J/m$^2$) | 30 |
| Mode II fracture energy, $G_{f2}$ (J/m$^2$) | 90 |
| Normal contact penalty, $P_n$ (GPa) | 18 |
| Tangential contact penalty, $P_s$ (GPa) | 62.5 |
| Sample-platen friction coefficient, $k_1$ (-) | 0.1 |
| Sample friction coefficient, $k_2$ (-) | 0.7 |

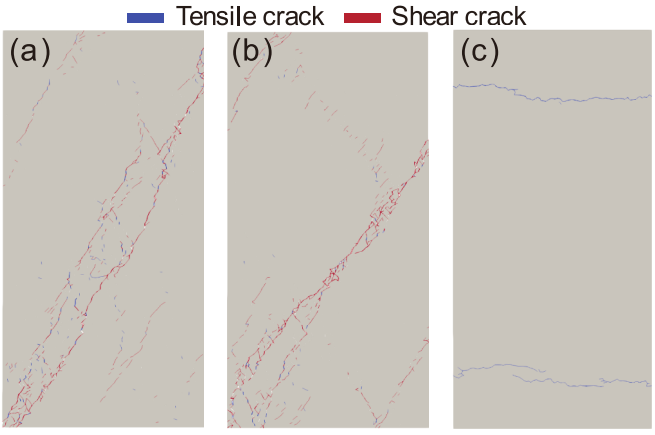


**Fig. 9.** Fracture patterns at failure in triaxial compression tests with (a) $\sigma_3 = 1$ MPa and (b) $\sigma_3 = 2$ MPa, and in (c) direct tension test.

are presented in Fig. 7b-d. It can be seen that the cFDEM simulated results are in good agreement with the analytical solution, which validates the accuracy of our proposed cFDEM for elastic deformation simulation using the node binding scheme.

### 3.2. Implementation accuracy of the strength criterion

To test the implementation accuracy of the Mohr-Coulomb and maximum tensile strength criterion in the proposed cFDEM, a series of triaxial compression and direct tension tests are performed on a rectangular plate presented in Fig. 8a-b, where the width and height of the specimen are 50 mm and 100 mm, respectively. The problem domain is composed of triangular elements with a mesh size of 1.0 mm, and the unstructured Delaunay triangulation mesh scheme is utilized. The input parameters of the problem are tabulated in Table 1, and the time step of all models is $1.2 \times 10^{-8}$ s. As shown in Fig. 8a, the axial compression loads are imposed on the specimen via two non-deformable platens moving in opposite directions at a constant velocity of 0.05 m/s, and the confining pressure applied on both sides of the specimen is increased gradually from 0 to the prescribed value via a time span of $3 \times 10^{-4}$ s. For direct tension tests, a constant velocity of 0.05 m/s is applied to the top and bottom of the specimen in both $y$ and -$y$ directions, respectively (Fig. 8b). Note that the selection of loading rates for the problem fully considers the effect of element size and also ensures an acceptable computation time (Tatone and Grasselli 2015).

The Mohr-Coulomb criterion in principal stress space is (Liu and Deng 2019)

$$\sigma_1 = \frac{2c\cdot cos\varphi}{1-sin\varphi} + \frac{1+sin\varphi}{1-sin\varphi}\sigma_3 \tag{18}$$

where $c$ is the material cohesion, φ is the internal friction angle, and $\sigma_1$ and $\sigma_3$ are the maximum and minimum principal stresses, respectively. We vary the confining pressure ($\sigma_3$) on the two sides of the model from 1 MPa to 6 MPa with a step of 1 MPa (compression positive), and obtain the corresponding peak strength ($\sigma_1$). The simulated $\sigma_1$-$\sigma_3$ relations, together with the theoretical curve of the Mohr-Coulomb and maximum tensile strength criterion, are plotted in Fig. 8c, which demonstrates a great consistency between the two and thus verifies the capability of cFDEM in simulating tensile and shear failures of rocks. Typical fracture patterns at failure in the triaxial compression and direct tension tests are presented in Fig. 9, in which the triaxial compression tests exhibit obvious shear failure, and tensile cracks are initiated from the top and bottom of the specimen in the direct tension test. Note that we only show the microcracks with damage variable $d = 1$ in all failure patterns, and the crack types are determined by the failure modes mentioned in Section 2.3.

### 3.3. Symmetrical three-point bending test

The classic symmetric three-point bending test is conducted to validate the correctness of the proposed cFDEM for tensile fracture simulation. The model dimensions and setup are presented in Fig. 10a, where $D$ and $S$ ($S = 5D$) are respectively the height and width of the rectangle beam. A zero-aperture pre-existing fracture of length $a$ is fabricated vertically in the bottom middle of the beam (marked by red line). At the top middle point, a non-deformable loading ball with a downward velocity of 0.01 m/s is used to bend the beam. The parameters used for the model are tabulated in Table 2. The total simulation time is $4 \times 10^{-3}$ s, and time step $\Delta t$ is set to $1.0 \times 10^{-8}$ s. The mesh around the pre-existing fracture is refined, and the unstructured Delaunay triangulation mesh scheme is employed (see Fig. 10b).

We compare the proposed cFDEM model with the analytical solution in terms of Mode I fracture toughness, which in the cFDEM model can be obtained using (Lisjak et al. 2013)

$$K_1 = \sqrt{G_{f1} \times E} \tag{19}$$

where $E$ is Young's modulus, and $G_{f1}$ is Mode I fracture energy. The analytical solution of Mode I fracture toughness is given by (Brown and Srawley 1966)

$$K_1^{ref} = \frac{PL\sqrt{a}}{BD^2}\left[2.9 - 4.6\left(\frac{a}{D}\right) + 21.8\left(\frac{a}{D}\right)^2 - 37.6\left(\frac{a}{D}\right)^3 + 38.7\left(\frac{a}{D}\right)^4\right] \tag{20}$$

Here, $P$ is the peak load obtained by the contact force between the beam and the top loading ball, $B$ is the thickness of the beam (in the direction perpendicular to the paper and set as one unit here), $L$ denotes the span of the beam (distance between the two bottom balls), and we have $a =$ 50 mm, $D = 150$ mm and $L = 600$ mm.

The Mode I fracture toughness obtained based on the cFDEM simulation is 2.344 MPa$\sqrt{\text{m}}$, which is very close to the analytical solution (2.313 MPa·$\sqrt{\text{m}}$), with a deviation of around ~ 1.32 %. This demonstrates that the proposed cFDEM can effectively simulate the Mode I fracture generation. It is worth noting that the error between numerical and analytical fracture toughness can be further reduced using a more refined mesh around the pre-existing fracture tips, and the effect of Mode II fracture energy on numerical results is not considered in this case. The cFDEM simulated fracture patterns are shown in Fig. 10c-d, where the newly generated fracture is marked in blue. It can be observed that the new fracture is initiated from the tip of the pre-existing fracture, and then propagates upwards with increasing loading. This is consistent with the previous studies (An et al. 2021; Yang et al. 2021), and thus

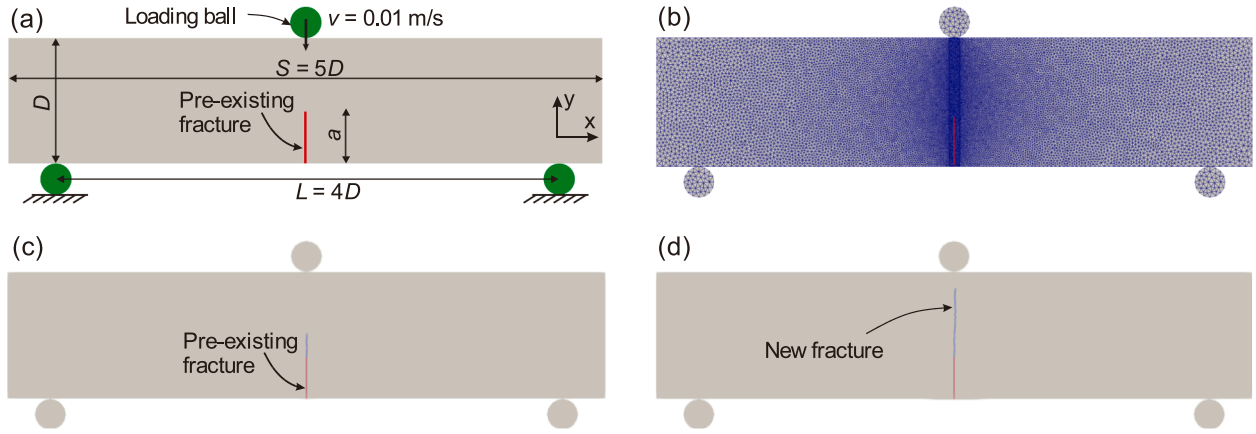


**Fig. 10.** (a) Geometry and (b) mesh of the model for the symmetrical three-point bending test. Fracture patterns in the symmetrical three-point bending test simulated in the proposed cFDEM at different timestamps: (c) $2 \times 10^{-3}$ s and (d) $3 \times 10^{-3}$ s.

**Table 2**
Input parameters in cFDEM model for the symmetrical three-point bending test.

| Input parameters | Values |
|---|---|
| Young's modulus, $E$ (GPa) | 26.5 |
| Bulk density, ρ (kg/m$^3$) | 2333 |
| Poisson's ratio, $\nu$ | 0.19 |
| Viscous damping coefficient, η (kg/m·s) | 6500 |
| Tensile strength, $f_t$ (MPa) | 3 |
| Cohesion, $c$ (MPa) | 15 |
| Internal friction angle, φ (°) | 27 |
| Mode I fracture energy, $G_{f1}$ (J/m$^2$) | 2 |
| Mode II fracture energy, $G_{f2}$ (J/m$^2$) | 20 |
| Normal contact penalty, $P_n$ (GPa) | 265 |
| Tangential contact penalty, $P_s$ (GPa) | 265 |
| Sample-ball friction coefficient, $k_1$ (-) | 0.1 |
| Sample friction coefficient, $k_2$ (-) | 0.7 |

validates the capability of the proposed cFDEM in tensile fracture simulation.

### 3.4. Asymmetric double-notched tensile test

An asymmetric double-notched tensile test is designed to simulate multiple fracture initiation and propagation under tensile loadings. The model has dimensions of 40 mm × 40 mm (width × height), containing two 8 mm long zero-aperture pre-existing fractures located horizontally and asymmetrically with respect to the model center (see Fig. 11a). The mesh around the two fractures is refined, and the unstructured Delaunay triangulation mesh scheme is employed (Fig. 11b). The top and bottom boundaries are pulled outwards at a velocity of 0.01 m/s. The mechanical parameters for the asymmetric double-notched tensile test are shown in Table 3, and the total simulation time is $3.6 \times 10^{-4}$ s, with a

**Table 3**
Input parameters in cFDEM model for asymmetric double-notched tensile test.

| Input parameters | Values |
|---|---|
| Young's modulus, $E$ (GPa) | 30 |
| Bulk density, ρ (kg/m$^3$) | 2700 |
| Poisson's ratio, $\nu$ | 0.27 |
| Viscous damping coefficient, η (kg/m·s) | 1000 |
| Tensile strength, $f_t$ (MPa) | 3 |
| Cohesion, $c$ (MPa) | 12 |
| Internal friction angle, φ (°) | 28 |
| Mode I fracture energy, $G_{f1}$ (J/m$^2$) | 1 |
| Mode II fracture energy, $G_{f2}$ (J/m$^2$) | 5 |
| Normal contact penalty, $P_n$ (GPa) | 300 |
| Tangential contact penalty, $P_s$ (GPa) | 300 |
| Sample friction coefficient, $k$ (-) | 0.7 |

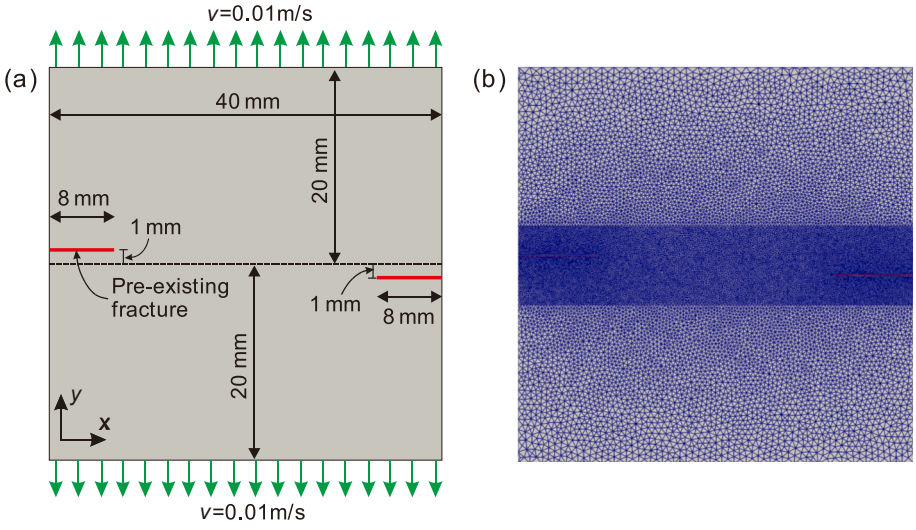


**Fig. 11.** The model of double-notched asymmetric tensile test. (a) Model geometry. (b) Mesh.

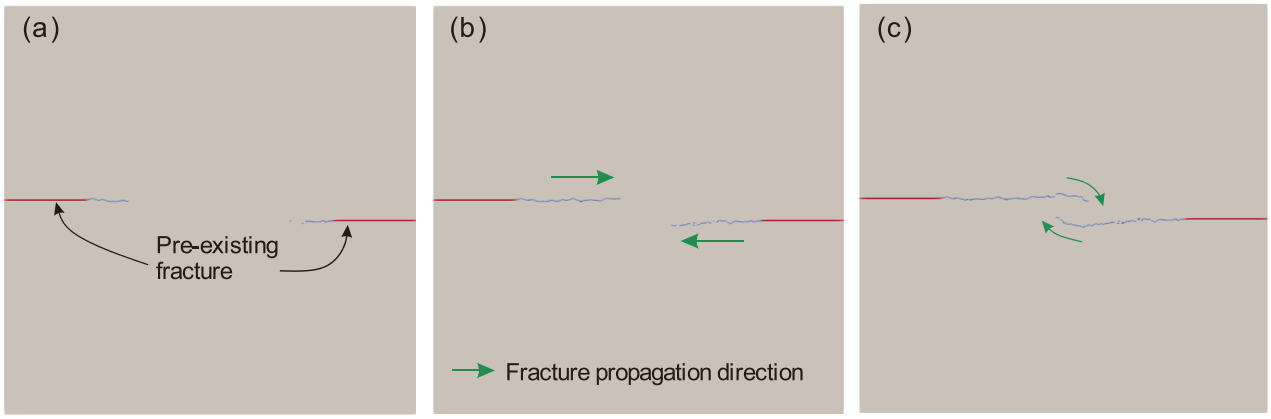


**Fig. 12.** Fracture pattern evolution in the double-notched asymmetric tensile test simulated in the proposed cFDEM at three different timestamps: (a) $1.08 \times 10^{-4}$ s, (b) $1.2 \times 10^{-4}$ s, and (c) $2.3 \times 10^{-4}$ s.

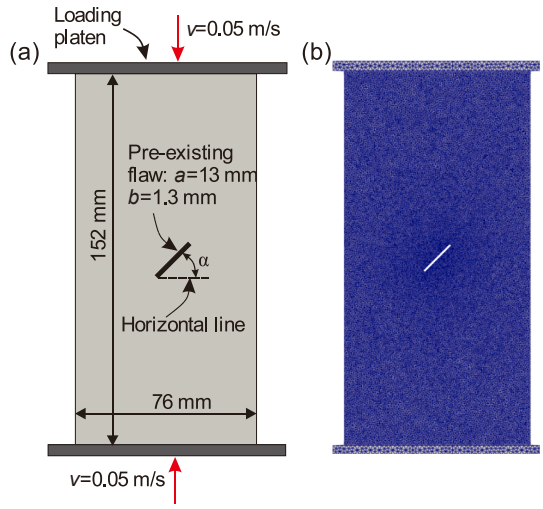


**Fig. 13.** The uniaxial compression test model with a pre-existing flaw. (a) Model geometry. (b) Mesh. The α is the inclination angle of the pre-existing flaw (counted anti-clockwise from the right). The length and thickness of the pre-existing flaw are denoted by *a* and *b*, respectively.

**Table 4**
Comparison of macroscopic material properties obtained from physical experiments and cFDEM simulations.

| Parameters | Physical experiment | cFDEM |
|---|---|---|
| Young's modulus, $E$ (GPa) | 5.96 | 5.96 |
| Poisson's ratio, $\nu$ | 0.15 | 0.15 |
| Tensile strength (MPa) | 3.2 | 3.1 |
| Uniaxial compressive strength (MPa) | 33.85 | 33.72 |

time step of $\Delta t = 3.0 \times 10^{-9}$ s.

The simulated fracture patterns at three different timestamps are shown in Fig. 12, where the pre-existing and newly generated fractures are marked as red and blue, respectively. The generated fractures are initiated from the tips of the pre-existing fractures (Fig. 12a), and continue to propagate along the horizontal direction toward the model center (Fig. 12b). Then, the propagation paths of fractures turn along the direction of maximum tensile stress, and the two fracture tips are attracted by each other (Fig. 12c), which would yield fracture coalescence as the loading continues. The fracture patterns are in good agreement with the previous results (Moës et al. 2011; Molnár and Gravouil 2017; Xu and Xie 2021), which verifies that the proposed cFDEM can adequately simulate multiple fracture initiation and propagation.

### 3.5. Uniaxial compression test with a pre-existing flaw

In this case, two uniaxial compression tests are performed to validate the capability of the proposed cFDEM in simulating fracture initiation and propagation in models with a pre-existing flaw. The models have dimensions of 76 mm × 152 mm (width × height), and each contains a 13 mm long and 1.3 mm thick pre-existing flaw with an inclination angle α (α = 30° and 45°, counted anti-clockwise from the right) (see Fig. 13). Axial compression loads are imposed on the top and bottom of each specimen through two non-deformable platens moving in opposite directions at a constant velocity of 0.05 m/s. Each model consists of ~ 43,000 triangular elements with an element size of 0.75 mm, and the unstructured Delaunay triangulation mesh scheme is also utilized. Again, the selection of loading rate and mesh size ensures reasonable simulation results.

In order to reliably compare the simulated fracture propagation patterns in the above models with those in similar laboratory physical experiments, we first conduct a series of regular uniaxial compression and Brazilian tension tests in cFDEM (not shown here due to space limitations) to find the appropriate input mechanical parameters that guarantee the consistency of material behavior in our simulations with the existing laboratory tests (e.g., Wong and Einstein 2009). The model input parameters are finally chosen as follows: Young's modulus $E$ = 5.96 GPa, Poisson's ratio $\nu = 0.15$, bulk density $\rho = 1540$ kg/m$^3$, viscous damping coefficient $\eta = 1700$ kg/m·s, tensile strength $f_t = 3$ MPa, cohesion $c = 8.8$ MPa, internal friction angle $\varphi = 33°$, Mode I fracture energy $G_{f1} = 2$ J/m$^2$, Mode II fracture energy $G_{f2} = 10$ J/m$^2$, normal contact penalty $P_n = 60$ GPa, tangential contact penalty $P_s = 100$ GPa, and time step $\Delta t = 2.0 \times 10^{-8}$. When using these input parameters, as shown in Table 4, the macroscopic material properties such as Young's modulus, Poisson's ratio, uniaxial compressive strength and tensile strength obtained from the cFDEM simulations are very close to the laboratory results, which lays a solid foundation for further investigation of fracture initiation and propagation.

The fracture patterns obtained from the cFDEM simulations and laboratory experiments (using the same material as in the above laboratory uniaxial compression and Brazilian tension tests) (Zhang and Wong 2011) for the models with a pre-existing flaw are compared in Fig. 14. It can be observed that wing cracks are first initiated from the two tips of the pre-existing flaw, and then propagate along the axial stress direction. Obviously, for the two cases (α = 30° and 45°), the fracture propagation paths obtained from our simulations are consistent with the earlier experimental observations (Zhang and Wong 2011).

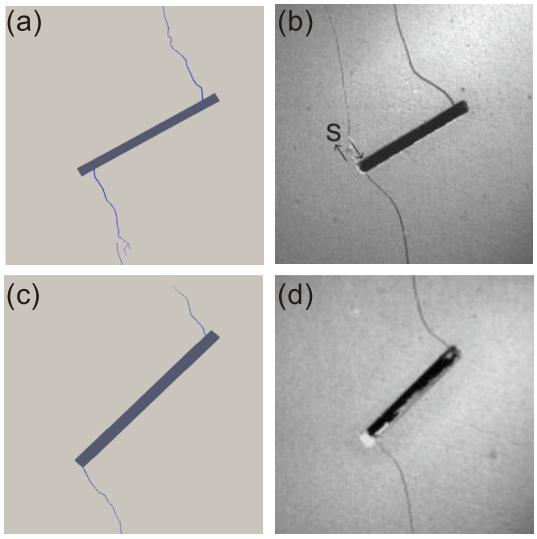


**Fig. 14.** Comparison of fracture propagation between cFDEM simulations and laboratory experiments for models with a flaw of different inclination angles. (a) cFDEM simulation results (α = 30°). (b) Laboratory experiment results (α = 30°) (Zhang and Wong 2011). (c) cFDEM simulation results (α = 45°). (d) Laboratory experiment results (α = 45°) (Zhang and Wong 2011).

## 4. Comparisons with the conventional dFDEM

In this section, three typical cases are employed to demonstrate the advantages of the proposed cFDEM compared with the conventional dFDEM from the aspects of simulated material stiffness, fracture aperture and computational efficiency.

### 4.1. Material stiffness

As mentioned in previous works (e.g., Fan and Tadmor 2019; Ghosh et al. 2019; Papoulia et al. 2003), the utilization of ICZM in dFDEM can reduce the overall effective modulus of materials (i.e., artificial compliance). Here, a square plate with a size of 30 mm (Fig. 15a) is employed to elucidate the material stiffness reduction in dFDEM before fracture onset and further check the correctness of the proposed cFDEM for elastic deformation simulation. The plate is assumed to be homogeneous and isotropic. Again, we gradually increase the tensile loads acting on both the top and bottom boundaries to σ = 1.0 MPa via a time span of 9 × $10^{-4}$ s and then maintain them unchanged. The loading condition guarantees that the model is under quasi-static condition, and the loads are small so that no fracture will be initiated. Here, we use Young's modulus $E$ = 30 GPa, Poisson's ratio $\nu$ = 0.27, bulk density ρ = 2700 kg/$m^3$, viscous damping coefficient η = 3050 kg/m·s, tensile strength $f_t$ = 18 MPa, cohesion $c$ = 45 MPa, and internal friction angle φ = 30° in the simulations. The model consists of 29,584 triangular elements with an average element size of 0.35 mm.

The material stiffness reduction in dFDEM is caused by the stiffness difference between solid finite elements and intrinsic cohesive elements in the intact regions (represented by the corresponding curve slope shown in Fig. 1d). Generally, the stiffness of an intrinsic cohesive element prior to fracture onset is controlled by the penalty parameters, which are usually chosen to be around 10–100 times of the Young's modulus $E$ of finite elements, and the larger the penalty parameters are, the stiffer the intrinsic cohesive elements will be (Fukuda et al. 2019). To compare the difference between dFDEM and the proposed cFDEM in terms of simulated material stiffness, we vary the ratio ($N$) between the intrinsic cohesive element penalty parameters and the prescribed Young's modulus of finite elements ($E$ = 30 GPa here) from 10 to 100, and calculate the ratio between the simulated macroscopic effective Young's modulus of each model ($E_{eff}$) and the prescribed Young's modulus of finite elements, i.e., $E_{eff}/E$. For convenience, we use a normal penalty parameter of the intrinsic cohesive elements equal to the tangential penalty, and this will also be used in Section 4.2. $E_{eff}$ can be obtained by the slope of the simulated tensile stress–strain curve in each numerical model. Note that the axial stress is obtained by averaging the normal stress components in the $y$ direction ($\sigma_y$) at five monitoring points (see green dots in Fig. 15a); similarly, the axial strain is determined by averaging the displacement variances in the $y$ direction at the monitoring points.

The ratio $E_{eff}/E$ with respect to $N$ is shown in Fig. 15b, which effectively demonstrates an overall material stiffness reduction in dFDEM, i.e., $E_{eff}/E < 1$. This is consistent with the previous statements (Tatone and Grasselli 2015). It can be observed that $E_{eff}/E$ gradually increases with the increment of $N$, but still less than one even for a very large $N$ (i.e., a very large intrinsic cohesive element stiffness). Theoretically, the overall material stiffness in dFDEM has no reduction only when the intrinsic cohesive element penalty tends to be infinity; however, in practice, too large a cohesive penalty could lead to spurious traction force oscillations, which may yield erroneous fracture simulation results (Borst et al. 2006). Although this problem can be alleviated by decreasing the time

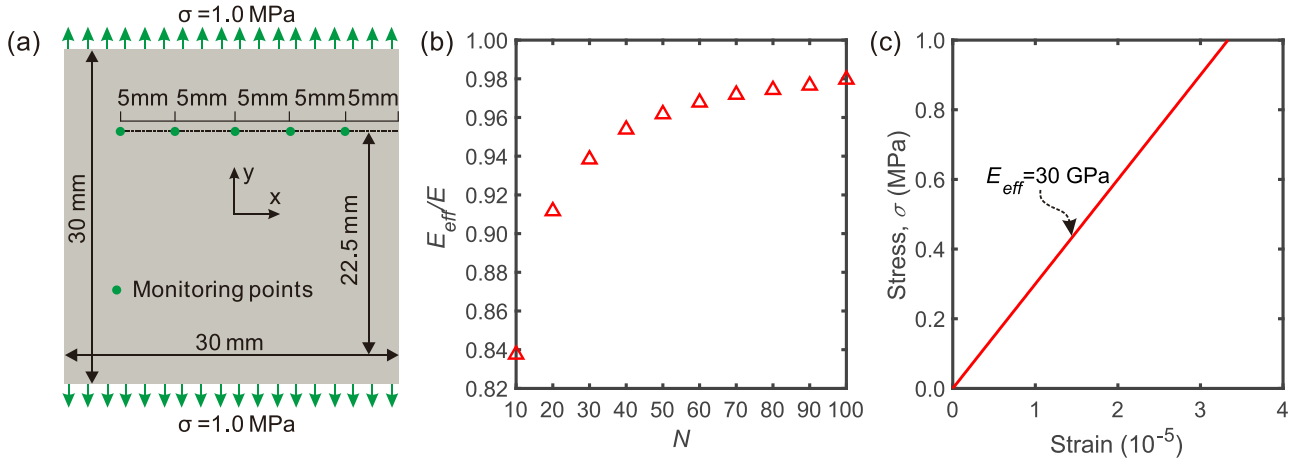


**Fig. 15.** (a) Model setup for simulated material stiffness comparison. (b) The ratio $E_{eff}$ /$E$ varies with $N$ in dFDEM. (c) Stress–strain curve under tensile loading in cFDEM. The $E_{eff}$ denotes the effective modulus obtained from simulations, and $E$ represents the prescribed Young's modulus of finite elements. The variable $N$ denotes the ratio between the intrinsic cohesive element penalty parameter to the Young's modulus of finite elements, which varies from 10 to 100. The stress and strain in the model are monitored with time at five monitoring points (marked by green dots in Fig. 15a). (For interpretation of the references to colour in this figure legend, the reader is referred to the web version of this article.)

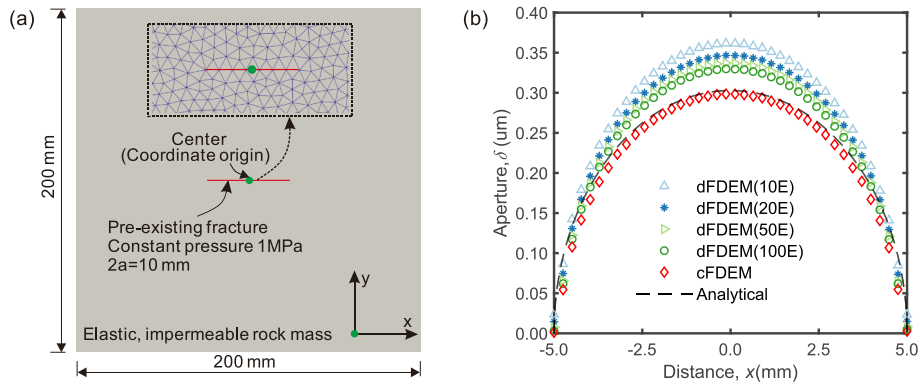


**Fig. 16.** (a) Model setup for fracture aperture simulation. (b) Distribution of fracture apertures for cFDEM, dFDEM and the analytical solution. The center of the specimen, the pre-existing fracture, and the origin of the coordinate system coincide and are denoted by a green dot. (For interpretation of the references to colour in this figure legend, the reader is referred to the web version of this article.)

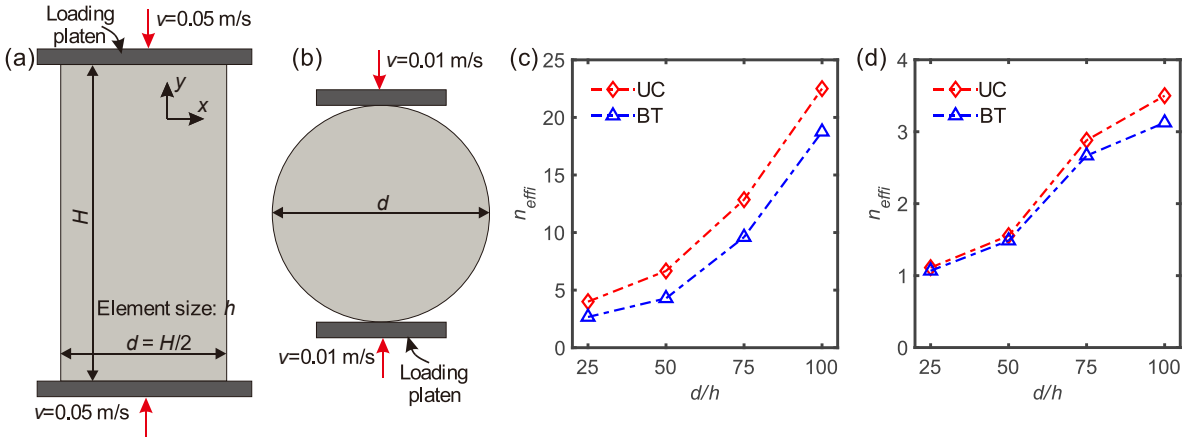


**Fig. 17.** Model geometry of (a) uniaxial compression (UC) test and (b) Brazilian tension (BT) test. Comparison of the computational efficiency between cFDEM and dFDEM with various element sizes using (c) brute-force contact activation and (d) dynamic contact activation. $H$ denotes the height of the rectangle specimen; $d$ represents the width of the rectangle specimen and the diameter of the Brazilian disc; $h$ is the element size.

**Table 5**
Input parameters of cFDEM and dFDEM for computational efficiency comparison (note that the "*" denotes the input parameter only required in dFDEM).

| Input parameters | cFDEM | dFDEM |
|---|---|---|
| Young's modulus, $E$ (GPa) | 12.5 | 12.5 |
| Bulk density, ρ (kg/m$^3$) | 2400 | 2400 |
| Poisson's ratio, $\nu$ | 0.25 | 0.25 |
| Tensile strength, $f_t$ (MPa) | 2.0 | 2.0 |
| Cohesion, $c$ (MPa) | 7.0 | 7.0 |
| Internal friction angle, φ (°) | 27 | 27 |
| Mode I fracture energy, $G_{f1}$ (J/m$^2$) | 30 | 30 |
| Mode II fracture energy, $G_{f2}$ (J/m$^2$) | 90 | 90 |
| Normal contact penalty, $P_n$ (GPa) | 18 | 18 |
| Tangential contact penalty, $P_s$ (GPa) | 62.5 | 62.5 |
| Sample-platen friction coefficient, $k_1$ (-) | 0.1 | 0.1 |
| Sample friction coefficient, $k_2$ (-) | 0.7 | 0.7 |
| Cohesive penalty*, $P_f$ (GPa) | – | 125 |

step ($\Delta t$), the computation cost will then increase substantially (Tatone and Grasselli 2015). While for the proposed cFDEM, as shown in Fig. 15c, the simulated effective Young's modulus is 30 GPa, which is the same as the prescribed Young's modulus for finite elements, i.e., no material stiffness reduction occurs in our cFDEM model.

It is worth noting that we use a linear stress–strain relationship for the simplicity of model validation (which explains the linear stress–-strain curve in Fig. 15c). Other constitutive laws can also be readily implemented under the framework of our proposed cFDEM. Additionally, except for contact penalty parameters, all other input parameters required in cFDEM can be directly obtained from laboratory experiments. While in the conventional dFDEM, parameters like intrinsic cohesive element penalty, which may affect the simulation results such as uniaxial compressive strength and the overall Poisson's ratio, can only be obtained by "trial and error" through careful and time-consuming calibrations with laboratory experiments. Any inappropriate selection of these so-called "numerical parameters" could reduce the accuracy of the simulation results in dFDEM (Liu and Deng 2019; Tatone and Grasselli 2015). Fortunately, in cFDEM, the significant reduction of the number of required numerical input parameters enhances its applicability, accuracy, efficiency and robustness for rock fracturing simulation.

### 4.2. Fracture aperture

It is well known that the variation of fracture aperture has great impacts in many applications such as the accuracy of hydraulic fracturing simulation. To check the robustness of the proposed cFDEM for fracture aperture simulation and to compare the results with dFDEM, a homogeneous and isotropic rock model with dimensions of 200 mm × 200 mm (width × height) is established (Fig. 16a). The rock contains a pre-existing fracture in the middle with zero initial aperture. The internal fluid, acting on the two walls of the fracture, is increased gradually from 0 to the prescribed value $P = 1$ MPa via a time span of $6 \times 10^{-4}$ s. The fluid pressure is small so that no new fractures will be initiated,

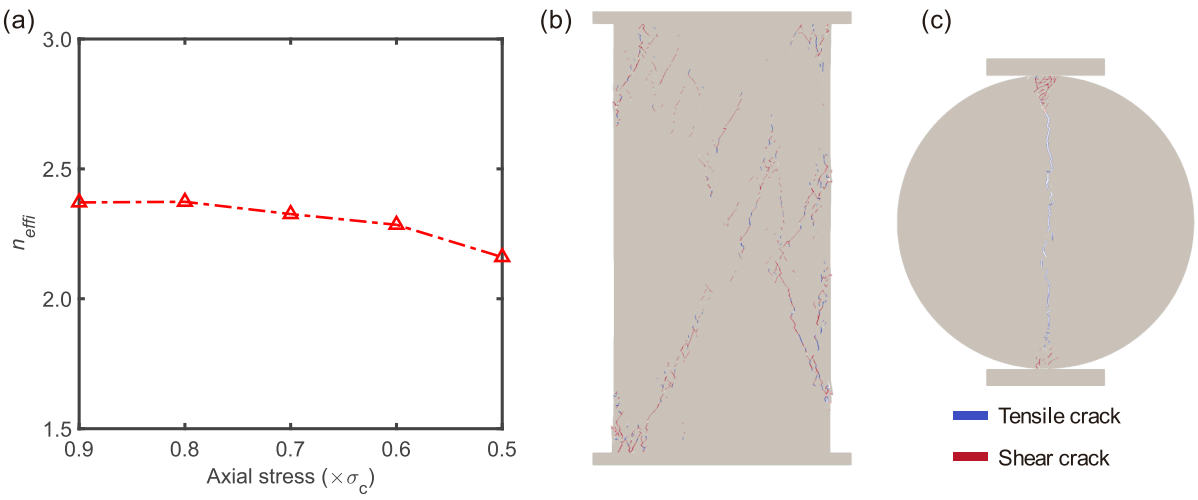


**Fig. 18.** (a) Comparison of the computational efficiency between cFDEM and dFDEM (using dynamic activation contact) under different axial stress (for the uniaxial compression test with $d/h = 75$). Fracture patterns at failure for (b) uniaxial compression test and (c) Brazilian tension test with $d/h = 75$. The peak stress is represented by $\sigma_c$.

and for simplicity, the rock is assumed to be impermeable. Upon the model reaching equilibrium, the apertures along the fracture are extracted for comparison. The following key rock parameters are used in the model: Young's modulus $E = 30$ GPa, bulk density $\rho = 1540$ kg/m$^3$, Poisson's ratio $\nu = 0.27$, and viscous damping coefficient $\eta = 4800$ kg/m·s. The model consists of 34,222 triangular elements with an average element size of 0.268 mm.

The analytical solution for the aperture along the fracture under the plane stress condition is given by (Lisjak et al. 2017)

$$\delta(x) = \frac{4P(1-\nu^2)}{E}\left(a^2 - x^2\right) \tag{21}$$

where $a = 5$ mm is the half-length of the pre-existing fracture, and $x$ represents the horizontal distance from the fracture center. The center of the specimen coincides with the origin of the $x$-$y$ coordinate system. As shown in Fig. 16b, the simulated fracture aperture in cFDEM is in good agreement with the analytical solution. While in general, the fracture aperture generated in dFDEM is larger than the analytical solution, and we speculate that this is still caused by the material stiffness reduction in dFDEM. To further investigate the effect of intrinsic cohesive element stiffness on fracture aperture simulation in dFDEM, we use four penalty values, i.e., 10, 20, 50 and 100 times the rock's Young's modulus, for the cohesive elements. The relative deviations of fracture aperture between the dFDEM simulated results and the analytical solution at $x = 0$ mm are respectively 19 %, 14 %, 11 % and 8 % for the four cohesive element penalty values. Although such fracture aperture deviation in dFDEM can be reduced with the increasing cohesive element stiffness, again, a large cohesive element penalty parameter could lead to stress oscillations and cause numerical instability (Borst et al. 2006). This confirms the inappropriateness of dFDEM for fracture aperture simulation during fluid injection. Consequently, the current applications of dFDEM in hydro-mechanical coupling simulation may yield biased fluid flow results due to the sensitivity of fluid pressure to fracture aperture, in which the fluid flow is proportional to the third power of fracture aperture and the fluid pressure is updated based on the net fluid flow (Lisjak et al. 2017; Yan and Jiao 2018; Yan et al. 2018).

### 4.3. Computational efficiency

As mentioned earlier, due to the participation of cohesive elements in computation from the beginning, the computational cost of dFDEM is significant. Here, we perform a series of uniaxial compression (UC) and Brazilian tension (BT) tests to compare the computational efficiency between dFDEM and the proposed cFDEM. Both types of tests use the same models presented in Fig. 17a-b, respectively: for the uniaxial compression tests, the model geometry $H$ and $d$ are respectively 100 mm and 50 mm; for the Brazilian tension tests, the model diameter is $d = 50$ mm. The axial loads are imposed on the specimens through two non-deformable platens moving inwards at a constant velocity. The velocities for uniaxial compression and Brazilian tension tests are 0.05 m/s and 0.01 m/s, respectively. Note that the selection of loading rates can ensure the quasi-static loading of the model (Liu and Deng 2019). The key input parameters of the specimens are tabulated in Table 5. It should be noted again that the cohesive element penalty parameters are only required in dFDEM.

For convivence, we define a variable

$$n_{effi} = \frac{T_d}{T_c} \tag{22}$$

to denote the ratio of the computing time needed between dFDEM and cFDEM upon specimens reaching the peak strength for both tests. For each type of test, we vary the element size $h$ to form different models and record the corresponding computation time. For dFDEM, both the original brute-force contact activation (Munjiza 2004) and new dynamic contact activation (Fukuda et al. 2021) schemes are considered. The former represents that all finite elements are added to the contact lists from the onset of the simulation, whereas in the latter, only finite elements connected to the newly broken cohesive elements participate in the contact processing. As shown in Fig. 17c-d, with the increase of $d/h$, i.e., a decrease of element size and thus an increase in the number of finite elements, the efficiency index $n_{effi}$ increases for both the brute-force contact activation (Fig. 17c) and dynamic contact activation schemes (Fig. 17d). Compared to the original dFDEM using brute-force contact activation, the computational efficiency of the proposed cFDEM increases nearly exponentially for both the uniaxial compression and Brazilian tension tests and reaches around 20 times when $d/h = 100$ (Fig. 17c). Undoubtedly, the new dynamic contact activation is more efficient; as presented in Fig. 17d, the value of $n_{effi}$ is less significant ($n_{effi} \approx 3$ when $d/h = 100$). Nevertheless, the proposed cFDEM is still more efficient than dFDEM, and such computational efficiency improves noticeably with the increasing number of finite elements.

To further compare the computational efficiency between the proposed cFDEM using node binding scheme and the dFDEM using dynamic contact activation, we select five timestamps after the peak stress for the previous uniaxial compression test model with $d/h = 75$. The five timestamps correspond to the axial stress drops to 90 %, 80 %, 70 %, 60

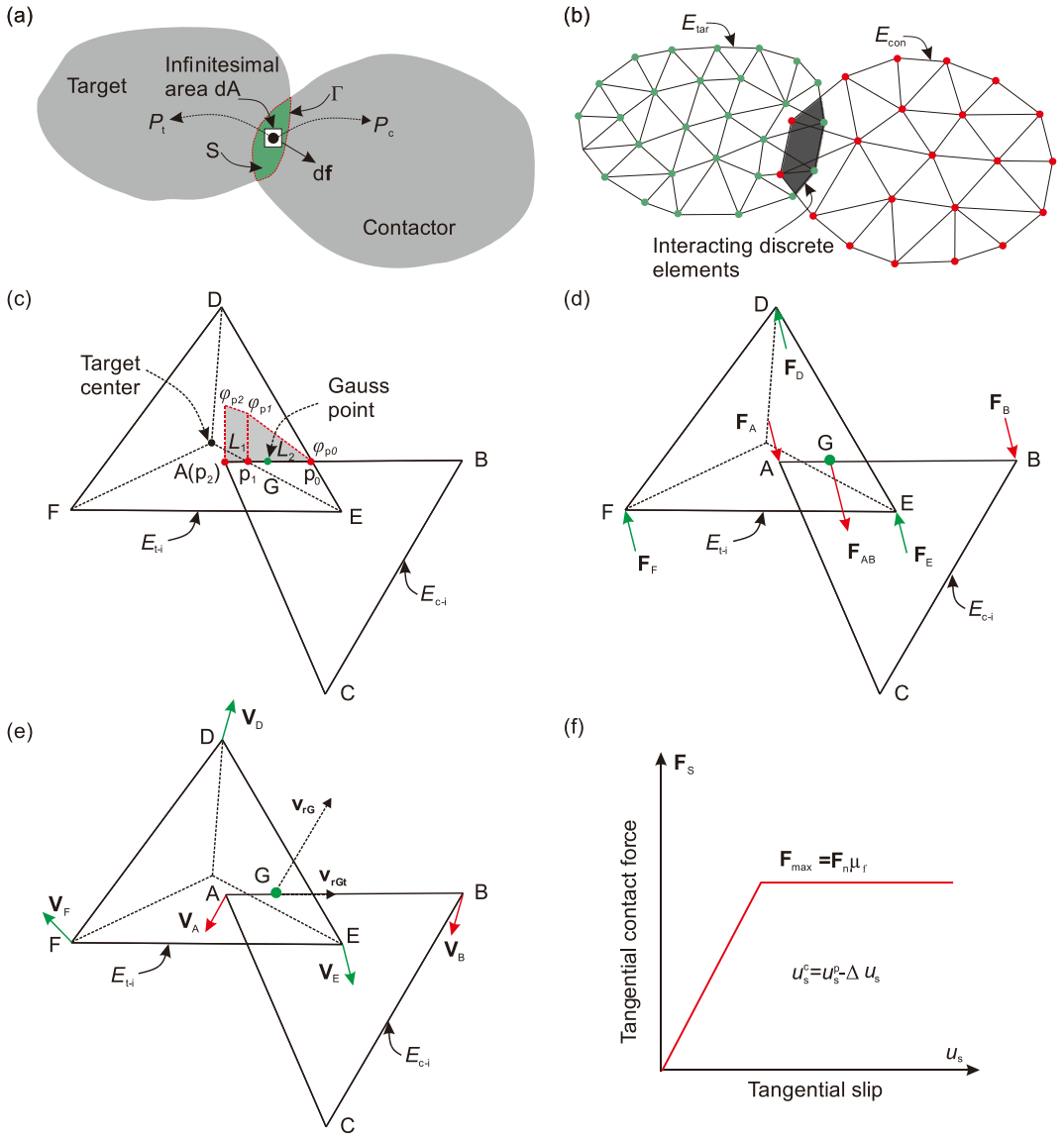


**Fig. A1.** Contact force calculation in 2D FDEM. (a) The repulsive force generated by a small penetration of two contacting solid domains. (b) Discretization of two rock matrix domains. (c) Distribution of potential of element $E_{t\text{-}i}$ on edge AB. (d) Equivalent nodal force. (e) The velocity of node and Gauss point. (f) Relationship between tangential slip and tangential contact force. $u_s^c$ and $u_s^p$ denote the tangential slip distance at the current and previous time, respectively.

% and 50 % of the peak stress, representing an increasing number of generated fractures. As shown in Fig. 18a, with the decrease of axial stress after peak, the computational efficiency $n_{effi}$ slowly decreases. This implies that the breakup of cohesive elements can reduce the relative computational efficiency of cFDEM due to frequent updates of master–slave lists. Fortunately, the computational efficiency of cFDEM is still more than twice that of dFDEM, indicating that the node binding scheme utilized in cFDEM can effectively enhance computational efficiency. Additionally, the fracture patterns at failure for the uniaxial compression test and Brazilian tension test with $d/h = 75$ are shown in Fig. 18b-c, where apparent shear failure occurs in the uniaxial compression test and tensile failure is initiated near the center of the Brazilian disc. Again, the crack types are identified by the failure modes mentioned in Section 2.3, and only the completely damaged microcracks are presented in Fig. 18b–c.

## 5. Conclusions

In this study, within the framework of cohesive element based FDEM, we have proposed a novel implementation of ECZM in 2D FDEM, i.e., a continuum-oriented FDEM (cFDEM), using an efficient node binding scheme for rock fracturing simulation. Using a strategy similar to the conventional ICZM-based dFDEM, the proposed cFDEM first discretizes the numerical model domain into finite elements and re-joints them with cohesive elements. Then, the approach binds the pre-discretized finite elements and suppresses the functionality of cohesive elements in the elastic stage, which guarantees the continuum behavior of materials prior to fracture onset. Upon the local stresses satisfying the strength criterion, the yield surfaces are dynamically embedded by invoking the pre-inserted cohesive elements to capture the strain-softening characteristics. In the meantime, the node binding lists are updated adaptively to achieve the explicit separation of yield or fracture surfaces and to prepare for the force calculation in the next iteration.

Five typical benchmark tests are conducted to validate the proposed cFDEM. The stress and displacement distributions obtained from the cFDEM simulation of a thick-wall cylinder under internal pressure are consistent with the analytical solution, which validates the accuracy of deformation and stress simulation in cFDEM prior to fracture onset. The cFDEM simulation results also agree well with the theoretical values for the Mohr-Coulomb and maximum tensile strength criterion, which

verifies the capability of the proposed cFDEM in simulating tensile and shear failure of rocks. Additionally, the crack propagation patterns obtained from the cFDEM simulation match well with the experimental observations, which further certifies that the proposed cFDEM can effectively simulate complex crack initiation and propagation on laboratory scales.

We further elucidate the advantages of the proposed cFDEM compared with the conventional dFDEM. In dFDEM, the stiffness reduction of material in the elastic stage is inevitable due to the different stiffness between intrinsic cohesive elements and finite elements. Fortunately, the cFDEM can always guarantee the correct modeling of elastic deformation. Additionally, the stiffness reduction of materials in dFDEM may also be responsible for the unreasonable fracture aperture simulation. On the contrary, the cFDEM simulated fracture aperture is in good agreement with the analytical solution. Importantly, the proposed cFDEM significantly enhances the computational efficiency compared with dFDEM, and this enhancement is more noteworthy for models with more elements.

Overall, the proposed cFDEM inherits the merits of both ICZM and ECZM, but avoids their shortcomings. Thus, it provides a novel solution for a more efficient and effective simulation of brittle material evolution from continuum to discontinuum. Additionally, the node binding scheme is parallelization friendly. Taking the space domain decomposition parallelization scheme for instance, because each node number of finite and cohesive element is independent in the node binding scheme, there is no need to update the topology of elements located in each computation domain (calculated by one processor) when fracturing occurs. This effectively reduces the complexity of parallelization and increases its ease of implementation. Also, the update of master–slave lists can be independently performed in each computation domain (Lukas et al. 2014). Therefore, we can readily achieve distributed parallelization using MPI (Message-Passing Interface) based on a space domain decomposition approach similar to that used for ICMZ-FDEM (Lukas et al. 2014).

However, here, we are not intended to solve the fundamental problem related to the utilization of ECZM in FDEM such as the "time discontinuity" problem pointed out in previous studies (Fukuda et al. 2021; Knight et al. 2020; Papoulia et al. 2003; Sam et al. 2005), in which the discontinuity of local nodal forces occurs before and after the insertion of a cohesive element due to the inconsistent constitutive models used for finite elements and cohesive elements in terms of nodal force calculation. Although efforts have been made to explore the smooth transition of local nodal force from finite elements to cohesive elements (Papoulia et al. 2003; Sam et al. 2005), they mainly only consider tensile failure, with the compressive-shear failure often ignored. It is worth noting that recently a non-differentiable energy-based cohesive interface method was proposed to alleviate spurious oscillations of local stress when a cohesive element is evoked (Hirmand and Papoulia 2019; Hirmand et al. 2021), which may provide a new perspective to solve the time-discontinuity problem. Unfortunately, this approach combines discontinuous Galerkin finite element and the principle of minimum energy, which may be incompatible with the current framework of FDEM. Additionally, the proposed framework may not be straightforwardly extended to 3D FDEM at the moment. Nevertheless, the strategy and philosophy of the node binding scheme also work for 3D. Further work, including the implementation and comparison of different strength criteria, as well as the extension of the node binding scheme to 3D rock fracturing simulation, will be reported in the near future.

## Declaration of Competing Interest

The authors declare that they have no known competing financial interests or personal relationships that could have appeared to influence the work reported in this paper.

## Data availability

Data will be made available on request.

## Acknowledgments

This work is supported by the Shenzhen Science and Technology Program (JCYJ20220530113612028) and the Guangdong Provincial Key Laboratory of Geophysical High-resolution Imaging Technology (2022B1212010002).

## Appendix A:. Contact detection and contact interaction

As sketched in Fig. A1a-b, each of the two rock matrix domains in touch is discretized into a series of triangular elements, then the contact between the two domains in 2D can be simplified into contact between a series of triangular finite elements along the two boundaries. These elements can be further grouped into a series of contact couples based on their relative positions, and rock matrix domains are denoted as the target ($E_{\text{tar}}$) and contactor ($E_{\text{con}}$), respectively. The overlapping area of $E_{\text{tar}}$ and $E_{\text{con}}$ is marked as $S$, and $dA$ denotes the infinitesimal overlapping area. The normal contact force $d\mathbf{f}$ of $dA$ is represented by (Munjiza 2004)

$$d\mathbf{f} = (\nabla\varphi_c(P_c) - \nabla\varphi_t(P_t))dA \tag{A.1}$$

where $P_c$ and $P_t$ denote the points located in the target and contactor area, respectively; the potentials of points $P_c$ and $P_t$ are denoted by $\varphi_c(P_c)$ and $\varphi_t(P_t)$, respectively. The total normal contact force of the overlapping area is calculated by (Munjiza 2004)

$$\mathbf{f}_c = \int_S (\nabla\varphi_c(P_c) - \nabla\varphi_t(P_t))\, dA \tag{A.2}$$

The target and contactor area consists of $m$ and $n$ triangular finite elements, respectively, then $\varphi_c(P_c)$ and $\varphi_t(P_t)$ can be obtained by a summation of potentials associated with individual finite elements (Munjiza 2004)

$$\left.\begin{aligned}\varphi_c &= \sum_{i=1}^{m}\varphi_c^i \\ \varphi_t &= \sum_{j=1}^{n}\varphi_t^j\end{aligned}\right\} \tag{A.3}$$

The total contact normal force can also be defined by (Munjiza 2004)

$$\mathbf{f}_c = \sum_{i=1}^{m}\sum_{j=1}^{n}\int_S \left(\nabla\varphi_c^i(P_c) - \nabla\varphi_t^j(P_t)\right) dA \tag{A.4}$$

By replacing the integration over the area with the equivalent integration over the boundary, the total normal contact force can be further simplified to (Munjiza 2004)

$$\mathbf{f}_{\mathrm{c}} = \sum_{i=1}^{m}\sum_{j=1}^{n}\int_{\Gamma}\mathbf{n}_{\Gamma}\left(\varphi_{\mathrm{c}}^{i}(P_{\mathrm{c}}) - \varphi_{\mathrm{t}}^{j}(P_{\mathrm{t}})\right)\, d\Gamma \tag{A.5}$$

where $\Gamma$ represents the boundary of the overlapping area of $E_{\mathrm{tar}}$ and $E_{\mathrm{con}}$; $\mathbf{n}_{\Gamma}$ denotes the outward unit normal to the boundary. For each triangular element, the point potential is defined as (Munjiza 2004)

$$\varphi_i(P) = P_{\mathrm{n}}\min\left\{\frac{3A_1}{A}, \frac{3A_2}{A}, \frac{3A_2}{A}\right\} \tag{A.6}$$

where $P_{\mathrm{n}}$ is the normal penalty parameter; $A_1$, $A_2$ and $A_3$ denote the areas of sub-triangle constituted by point $P$ and the three edges of the triangular element; $A$ is the area of element $E_{\mathrm{t\text{-}i}}$.

The contact tangential force is calculated based on the relative slipping displacement between contact couples, and is further updated using Coulomb's friction law. The relative velocity at Gauss point G ($\mathbf{V}_{\mathrm{rG}}$) is given by (Munjiza et al. 2011)

$$\mathbf{V}_{\mathrm{rG}} = \mathbf{V}_{\mathrm{cG}} - \mathbf{V}_{\mathrm{tG}} \tag{A.7}$$

where $\mathbf{V}_{\mathrm{cG}}$ and $\mathbf{V}_{\mathrm{tG}}$ are the velocities of the contactor and target element at action point G, respectively, which can be calculated by (Munjiza et al. 2011)

$$\mathbf{V}_{\mathrm{cG}} = N_{\mathrm{A}}\mathbf{V}_{\mathrm{A}} + N_{\mathrm{B}}\mathbf{V}_{\mathrm{B}} \tag{A.8}$$

and (Munjiza et al. 2011)

$$\mathbf{V}_{\mathrm{tG}} = N_{\mathrm{D}}\mathbf{V}_{\mathrm{D}} + N_{\mathrm{E}}\mathbf{V}_{\mathrm{F}} + N_{\mathrm{F}}\mathbf{V}_{\mathrm{F}} \tag{A.9}$$

where $\mathbf{V}_{\mathrm{A}}$, $\mathbf{V}_{\mathrm{B}}$, $\mathbf{V}_{\mathrm{D}}$, $\mathbf{V}_{\mathrm{E}}$ and $\mathbf{V}_{\mathrm{F}}$ are the node velocity shown in Fig. A1e. It should be noted that the total moment at the location of Gauss point G is zero. Then, the tangential relative displacement increment ($\Delta u$) within a timestep ($\Delta t$) is given by (Munjiza et al. 2011)

$$\Delta u = V_{\mathrm{rGt}}\Delta t \tag{A.10}$$

where $V_{\mathrm{rGt}}$ is the projection of $\mathbf{V}_{\mathrm{rG}}$ on edge AB. The contact tangential force can be updated incrementally by (Munjiza et al. 2011)

$$\mathbf{F}_s = \mathbf{F}_s^{t-\Delta t} - P_{\mathrm{s}}L_{\mathrm{c}}\Delta u \tag{A.11}$$

where $\mathbf{F}_{\mathrm{s}}$ and $\mathbf{F}_{\mathrm{s}}^{t-\Delta t}$ are contact tangential force at the current and previous time step; $P_{\mathrm{s}}$ is the tangential penalty parameter; $L_{\mathrm{c}}$ is the contact length. As presented in Fig. A1f, if$|\mathbf{F}_{\mathrm{s}}| \geqslant |\mathbf{F}_{\mathrm{n}}|\mu_{\mathrm{f}}$, the contact tangential force can be calculated based on Coulomb's friction law (Munjiza et al. 2011)

$$\mathbf{F}_{\mathrm{s}} = \frac{\mathbf{F}_{\mathrm{s}}}{|\mathbf{F}_{\mathrm{s}}|}|\mathbf{F}_{\mathrm{n}}|\mu_{\mathrm{f}} \tag{A.12}$$

where $\mathbf{F}_{\mathrm{n}}$ is the normal contact force, $\mu_{\mathrm{f}}$ is the contact friction coefficient. At the same time, the current tangential slip ($u_{\mathrm{s}}$) is updated by (Munjiza et al. 2011)

$$u_{\mathrm{s}} = \frac{|\mathbf{F}_{\mathrm{s}}|}{P_{\mathrm{s}}L_{\mathrm{c}}} \tag{A.13}$$

## References


Aliabadi, M.H., 1997. Boundary element formulations in fracture mechanics. Appl. Mech. Rev. 50 (2), 83–96.

An, H., Song, Y., Liu, H., Fang, C., 2021. FDEM Modelling of Rock fracture process during three-point bending test under quasistatic and dynamic loading conditions. Shock Vib. 1–21.

Anyfantis, K.N., Tsouvalis, N.G., 2012. A novel traction–separation law for the prediction of the mixed mode response of ductile adhesive joints. Int. J. Solids Struct. 49 (1), 213–226.

Belytschko, T., Moës, N., Usui, S., Parimi, C., 2001. Arbitrary discontinuities in finite elements. Int. J. Numer. Methods Eng. 50 (4), 993–1013.

Borst, R.d., Remmers, J.J.C., Needleman, A., 2006. Mesh-independent discrete numerical representations of cohesive-zone models. Eng. Fract. Mech. 73 (2), 160–177.

Brown, W., Srawley, J., 1966. Plane strain crack toughness testing of high strength metallic materials. Plane strain crack toughness testing of high strength metallic materials. ASTM International.

Camacho, G.T., Ortiz, M., 1996. Computational modelling of impact damage in brittle materials. Int. J. Solids Struct. 33 (20), 2899–2938.

Cundall, P.A., Strack, O.D.L., 1979. A discrete numerical model for granular assemblies. Geotechnique. 29 (1), 47–65.

Deng, P., Liu, Q., Huang, X., Bo, Y., Liu, Q., Li, W., 2021a. Sensitivity analysis of fracture energies for the combined finite-discrete element method (FDEM). Eng. Fract. Mech. 251, 107793.

Deng, P., Liu, Q., Huang, X., Liu, Q., Ma, H., Li, W., 2021b. Acquisition of normal contact stiffness and its influence on rock crack propagation for the combined finite-discrete element method (FDEM). Eng. Fract. Mech. 242, 107459.

Deng, P., Liu, Q., Huang, X., Ma, H., 2021c. A new hysteretic damping model and application for the combined finite-discrete element method (FDEM). Eng. Anal. Bound. Elem. 132, 370–382.

Deng, P., Liu, Q., Huang, X., Pan, Y., Wu, J., 2021d. FDEM numerical modeling of failure mechanisms of anisotropic rock masses around deep tunnels. Comput. Geotech. 142, 104535.

Duan, K., Ji, Y., Xu, N., Wan, Z., Wu, W., 2019. Excavation-induced fault instability: possible causes and implications for seismicity. Tunn. Undergr. Space Technol. 92, 103041.

Euser, B., Rougier, E., Lei, Z., Knight, E.E., Frash, L.P., Carey, J.W., Viswanathan, H., Munjiza, A., 2019. Simulation of fracture coalescence in granite via the combined finite-discrete element method. Rock Mech. Rock Eng. 52 (9), 3213–3227.
Fan, J., Tadmor, E.B., 2019. Rescaling cohesive element properties for mesh independent fracture simulations. Eng. Fract. Mech. 213, 89–99.
Francfort, G.A., Marigo, J.J., 1998. Revisiting brittle fracture as an energy minimization problem. J. Mech. Phys. Solids. 46 (8), 1319–1342.
Fukuda, D., Mohammadnejad, M., Liu, H., Zhang, Q., Zhao, J., Dehkhoda, S., Chan, A., Kodama, J.-I., Fujii, Y., 2019. Development of a 3D hybrid finite-discrete element simulator based on GPGPU-parallelized computation for modelling rock fracturing under quasi-static and dynamic loading conditions. Rock Mech. Rock Eng. 53 (3), 1079–1112.
Fukuda, D., Nihei, E., Cho, S.-H., Oh, S., Nara, Y., Kodama, J.-I., Fujii, Y., 2020. Development of a Numerical Simulator for 3-D dynamic fracture process analysis of rocks based on hybrid FEM-DEM using extrinsic cohesive zone model. Mater. Trans. 61 (9), 1767–1774.
Fukuda, D., Liu, H., Zhang, Q., Zhao, J., Kodama, J.-I., Fujii, Y., Chan, A.H.C., 2021. Modelling of dynamic rock fracture process using the finite-discrete element method with a novel and efficient contact activation scheme. Int. J. Rock Mech. Min. Sci. 138, 104645.
Ghosh, G., Duddu, R., Annavarapu, C., 2019. A stabilized finite element method for enforcing stiff anisotropic cohesive laws using interface elements. Comput. Meth. Appl. Mech. Eng. 348, 1013–1038.
Griffith, A.A., 1920. The phenomena of rupture and flow in solids. Philos. Trans. R. Soc., A. 221 (4), 163–198.
Han, H., Fukuda, D., Liu, H., Fathi Salmi, E., Sellers, E., Liu, T., Chan, A., 2020a. FDEM simulation of rock damage evolution induced by contour blasting in the bench of tunnel at deep depth. Tunn. Undergr. Space Technol. 103, 103495.
Han, H., Fukuda, D., Liu, H., Salmi, E.F., Sellers, E., Liu, T., Chan, A., 2020b. Combined finite-discrete element modelling of rock fracture and fragmentation induced by contour blasting during tunnelling with high horizontal in-situ stress. Int. J. Rock Mech. Min. Sci. 127, 104214.
Hirmand, M.R., Papoulia, K.D., 2019. Block coordinate descent energy minimization for dynamic cohesive fracture. Comput. Meth. Appl. Mech. Eng. 354, 663–688.
Hirmand, M.R., Vahab, M., Papoulia, K.D., Khalili, N., 2021. Energy minimization versus criteria-based methods in discrete cohesive fracture simulations. Comput. Mech. 68 (4), 845–860.
Jiang, H., Cai, Z., Zhao, H., 2020. Numerical study of hard rock breakage under indenter impact by the hybrid FDEM. Eng. Fract. Mech. 233 (5), 107068.
Ju, Y., Liu, P., Chen, J., Yang, Y., Ranjith, P.G., 2016. CDEM-based analysis of the 3D initiation and propagation of hydrofracturing cracks in heterogeneous glutenites. J. Nat. Gas Sci. Eng. 35, 614–623.
Junior, R.A.A., Cheng, L.Y., 2013. Brittle fracture and hydroelastic simulations based on moving particle simulation. CMES-Comp. Model. Eng. Sci. 95 (2), 87–118.
Knight, E.E., Rougier, E., Lei, Z., Euser, B., Chau, V., Boyce, S.H., Gao, K., Okubo, K., Froment, M., 2020. HOSS: an implementation of the combined finite-discrete element method. Comput. Part. Mech. 7, 765–787.
Lei, Q., Gao, K., 2018. Correlation between fracture network properties and stress variability in geological media. Geophys. Res. Lett. 45 (9), 3994–4006.
Lei, Q., Latham, J.-P., Xiang, J., 2016. Implementation of an empirical joint constitutive model into finite-discrete element analysis of the geomechanical behaviour of fractured rocks. Rock Mech. Rock Eng. 49 (12), 4799–4816.
Lei, Q., Gholizadeh Doonechaly, N., Tsang, C.-F., 2021a. Modelling fluid injection-induced fracture activation, damage growth, seismicity occurrence and connectivity change in naturally fractured rocks. Int. J. Rock Mech. Min. Sci. 138, 104598.
Lei, Z., Rougier, E., Knight, E.E., Zang, M., Munjiza, A., 2021b. Impact fracture and fragmentation of glass via the 3D combined finite-discrete element method. Appl. Sci. 11 (6), 2484.
Li, B.-X., Yu, S., Zhu, W.-S., Yang, L., Cai, W.-B., Xue, Y.-G., Li, Y., 2020. The crack coalescence mode and physical field evolutionary characteristics of a brittle material containing two 3-D parallel embedded flaws. Theor. Appl. Fract. Mech. 110, 103448.
Lisjak, A., Liu, Q., Zhao, Q., Mahabadi, O.K., Grasselli, G., 2013. Numerical simulation of acoustic emission in brittle rocks by two-dimensional finite-discrete element analysis. Geophys. J. Int. 195 (1), 423–443.
Lisjak, A., Grasselli, G., Vietor, T., 2014. Continuum–discontinuum analysis of failure mechanisms around unsupported circular excavations in anisotropic clay shales. Int. J. Rock Mech. Min. Sci. 65, 96–115.
Lisjak, A., Kaifosh, P., He, L., Tatone, B.S.A., Mahabadi, O.K., Grasselli, G., 2017. A 2D, fully-coupled, hydro-mechanical, FDEM formulation for modelling fracturing processes in discontinuous, porous rock masses. Comput. Geotech. 81, 1–18.
Lisjak, A., Mahabadi, O.K., He, L., Tatone, B.S.A., Kaifosh, P., Haque, S.A., Grasselli, G., 2018. Acceleration of a 2D/3D finite-discrete element code for geomechanical simulations using General Purpose GPU computing. Comput. Geotech. 100, 84–96.
Liu, Q., Deng, P., 2019. A numerical investigation of element size and loading/unloading rate for intact rock in laboratory-scale and field-scale based on the combined finite-discrete element method. Eng. Fract. Mech. 211, 442–462.
Liu, Q., Jiang, Y., Wu, Z., Qian, Z., Xu, X., 2018. Numerical modeling of acoustic emission during rock failure process using a Voronoi element based – explicit numerical manifold method. Tunn. Undergr. Space Technol. 79, 175–189.
Liu, H., Kang, Y., Lin, P., 2015. Hybrid finite–discrete element modeling of geomaterials fracture and fragment muck-piling. Int. J. Geotech. Eng. 9 (2), 115–131.
Lukas, T., Schiava D'Albano, G.G., Munjiza, A., 2014. Space decomposition based parallelization solutions for the combined finite–discrete element method in 2D. J. Rock Mech. Geotech. Eng. 6 (6), 607–615.
Mahabadi, O.K., Lisjak, A., Munjiza, A., Grasselli, G., 2012. Y-Geo: new combined finite-discrete element numerical code for geomechanical applications. Int. J. Geomech. 12 (6), 676–688.
Moës, N., Stolz, C., Bernard, P.E., Chevaugeon, N., 2011. A level set based model for damage growth: the thick level set approach. Int. J. Numer. Methods Eng. 86 (3), 358–380.
Mohammadnejad, M., Liu, H., Chan, A., Dehkhoda, S., Fukuda, D., 2018. An overview on advances in computational fracture mechanics of rock. Geosystem Eng. 24 (4), 206–229.
Molnár, G., Gravouil, A., 2017. 2D and 3D Abaqus implementation of a robust staggered phase-field solution for modeling brittle fracture. Finite Elem. Anal. Des. 130, 27–38.
Munjiza, A., 1992. Discrete elements in transient dynamics of fractured media. Swansea University.
Munjiza, A., 2004. The combined finite-discrete element method. John Wiley, London.
Munjiza, A., Andrews, K.R.F., 1998. NBS contact detection algorithm for bodies of similar size. Int. J. Numer. Methods Eng. 43 (1), 131–149.
Munjiza, A., Andrews, K.R.F., White, J.K., 1999. Combined single and smeared crack model in combined finite-discrete element analysis. Int. J. Numer. Methods Eng. 44 (1), 41–57.
Munjiza, A.A., Knight, E.E., Rougier, E., 2011. Computational mechanics of discontinua. Willey, London.
Munjiza, A., Lei, Z., Divic, V., Peros, B., 2013. Fracture and fragmentation of thin shells using the combined finite-discrete element method. Int. J. Numer. Methods Eng. 95 (6), 478–498.
Ortiz, M., Structures, 1988. Microcrack coalescence and macroscopic crack growth initiation in brittle solids. Int. J. Solids Struct. 24 (3), 231–250.
Papoulia, K.D., Sam, C.-H., Vavasis, S.A., 2003. Time continuity in cohesive finite element modeling. Int. J. Numer. Methods Eng. 58 (5), 679–701.
Sam, C.-H., Papoulia, K.D., Vavasis, S.A., 2005. Obtaining initially rigid cohesive finite element models that are temporally convergent. Eng. Fract. Mech. 72 (14), 2247–2267.
Shi, G.H., 1992. Discontinuous deformation analysis: a new numerical model for the statics and dynamics of deformable block structures. Eng. Comput. 9 (2), 157–168.
Shi, G.H., Goodman, R.E., 1985. Two dimensional discontinuous deformation analysis. Int. J. Numer. Anal. Methods Geomech. 9 (6), 541–556.
Silling, S.A., Askari, E., 2005. A meshfree method based on the peridynamic model of solid mechanics. Comput. Struct. 83 (17–18), 1526–1535.
Tatone, B.S.A., Grasselli, G., 2015. A calibration procedure for two-dimensional laboratory-scale hybrid finite–discrete element simulations. Int. J. Rock Mech. Min. Sci. 75, 56–72.
Timoshenko, S.P., Goodier, J.N., 1970. Theory of Elasticity. Int. J. Appl. Mech. 37 (3), 888.
Wang, B., Li, H., Shao, Z., Chen, S., Li, X., 2021. Investigating the mechanism of rock fracturing induced by high-pressure gas blasting with a hybrid continuum-discontinuum method. Comput. Geotech. 140, 104445.
Wei, C., Li, Y., Zhu, W., Li, S., Wang, S., Wang, H., 2020. Experimental observation and numerical investigation on propagation and coalescence process of multiple flaws in rock-like materials subjected to hydraulic pressure and far-field stress. Theor. Appl. Fract. Mech. 108, 102603.
Wong, L.N.Y., Einstein, H.H., 2009. Systematic evaluation of cracking behavior in specimens containing single flaws under uniaxial compression. Int. J. Rock Mech. Min. Sci. 46 (2), 239–249.
Xu, X.P., Needleman, A., 1993. Void nucleation by inclusion debonding in a crystal matrix. Model. Simul. Mater. Sci. Eng. 1 (2), 111–132.
Xu, X., Wang, D., Zang, M., Chen, S., 2022. Development of an intrinsic solid-shell cohesive zone model for impact fracture of windshield laminated glass. Int. J. Impact Eng. 163, 104187.
Xu, Z., Xie, W., 2021. Phase-field model for brittle fracture based on the inner-element edge-based smoothed finite method (IES-FEM). Eng. Fract. Mech. 254, 107919.
Yan, C., Jiao, Y.-Y., 2018. A 2D fully coupled hydro-mechanical finite-discrete element model with real pore seepage for simulating the deformation and fracture of porous medium driven by fluid. Comput. Struct. 196, 311–326.
Yan, C., Jiao, Y.-Y., Yang, S., 2018. A 2D coupled hydro-thermal model for the combined finite-discrete element method. Acta Geotech. 14 (2), 403–416.
Yan, C., Zheng, Y., Ke, W., Wang, G., 2021. A FDEM 3D moisture migration-fracture model for simulation of soil shrinkage and desiccation cracking. Comput. Geotech. 140, 104425.
Yan, C., Xie, X., Ren, Y., Ke, W., Wang, G., 2022. A FDEM-based 2D coupled thermal-hydro-mechanical model for multiphysical simulation of rock fracturing. Int. J. Rock Mech. Min. Sci. 149, 104964.
Yang, L., Yang, Y., Zheng, H., 2021. A phase field numerical manifold method for crack propagation in quasi-brittle materials. Eng. Fract. Mech. 241, 107427.
Zhang, X.-P., Wong, L.N.Y., 2011. Cracking processes in rock-like material containing a single flaw under uniaxial compression: a numerical study based on parallel bonded-particle model approach. Rock Mech. Rock Eng. 45 (5), 711–737.
Zhao, Q., Lisjak, A., Mahabadi, O., Liu, Q., Grasselli, G., 2014. Numerical simulation of hydraulic fracturing and associated microseismicity using finite-discrete element method. J. Rock Mech. Geotech. Eng. 6 (6), 574–581.
Zhao, Q., Tisato, N., Grasselli, G., Mahabadi, O.K., Lisjak, A., Liu, Q., 2015. Influence ofin situstress variations on acoustic emissions: a numerical study. Geophys. J. Int. 203 (2), 1246–1252.